Available online at www.sciencedirect.com
ScienceDirect
Comput. Methods Appl. Mech. Engrg. 351 (2019) 35–59
Computer methods in applied mechanics and engineering
www.elsevier.com/locate/cma

Fast, provably unconditionally energy stable, and second-order accurate algorithms for the anisotropic Cahn–Hilliard Model☆

Chuanjun Chen[a], Xiaofeng Yang[b,*]

[a] School of Mathematics and Information Sciences, Yantai University, Yantai 264005, China
[b] Department of Mathematics, University of South Carolina, Columbia, SC 29208, United States

Received 7 November 2018; received in revised form 14 March 2019; accepted 14 March 2019
Available online 25 March 2019

Highlights

- We propose a novel Stabilized-SAV approach for solving the anisotropic Cahn–Hilliard model.
- The scheme is linear, second-order accurate, provably unconditionally energy stable, and non-iterative.
- Three crucial linear stabilization terms are added to remove oscillations caused by anisotropy.
- One only need to solve three decoupled linear equations at each time step.
- We further prove the unconditional energy stabilities rigorously and present numerous simulations.

Abstract

In this paper, we consider numerical approximations for solving the anisotropic Cahn–Hilliard model. We combine the Scalar Auxiliary Variable (SAV) approach with the stabilization technique to arrive at a novel Stabilized-SAV approach, where three linear stabilization terms, which are shown to be crucial to remove the oscillations caused by the anisotropic coefficient, are added to enhance the stability while keeping the required accuracy. The schemes are very easy-to-implement and fast in the sense that all nonlinear terms are treated in a semi-explicit way, and one only needs to solve three decoupled linear equations with constant coefficients at each time step. We further prove the unconditional energy stabilities rigorously and present numerous 2D and 3D numerical simulations to demonstrate the stability and accuracy.

Keywords: Phase-field; Linear; Stabilized-SAV; Second-order; Anisotropy; Cahn–Hilliard

☆ The work of C. Chen was supported by the NSFC-11771375 and NSFC-11571297, Shandong Province Natural Science Foundation ZR2018MAQ008. The work of X. Yang was partially supported by the National Science Foundation under grant numbers DMS-1720212, DMS-1818783, and USC ASPIRE I Track-III/IV Fund.
* Corresponding author.
E-mail addresses: cjchen@ytu.edu.cn (C. Chen), xfyang@math.sc.edu (X. Yang).

https://doi.org/10.1016/j.cma.2019.03.030
0045-7825/

1. Introduction

In this paper, we consider numerical approximations for solving the anisotropic Cahn–Hilliard model proposed by Torabi et al. in [1,2], where a sufficiently big anisotropic coefficient is introduced to simulate the formation of faceted pyramids on nanoscale crystal surfaces. When the anisotropic coefficient vanishes, the system degenerates to the well-known Cahn–Hilliard model, that is a representative equation of the phase field method, or called diffusive interface method. Such a method has been extensively studied and applied to resolve the motion of free interfaces between multiple material components, see [3–10].

Comparing to the isotropic Cahn–Hilliard model, in addition to the stiffness issue from the interfacial width, the specialty of the anisotropic system is that there exists a strong anisotropic coefficient $\gamma(\frac{\nabla\phi}{|\nabla\phi|})$ that can induce large oscillations numerically so that the complexity of algorithm development is increased to a large extent. Hence there existed very few successful attempts in designing efficient and provably energy stable schemes for this model. In [1,2], the authors used the fully-implicit method to discretize the nonlinear terms. Its energy stability is not provable, and the computational cost is high due to its nonlinear nature. In [11], a first-order scheme is developed based on the linear stabilization approach where all nonlinear terms are treated explicitly. Some extra linear stabilizers are added to enhance the stability. However, the energy stability is not provable for the anisotropic case even though the scheme is quite efficient and stable that allows for the large time step in computations. In [12], the authors applied the convex-splitting approach for solving this model, however, their scheme is only provably energy stable for the isotropic case. In [13], the authors proposed a second-order scheme that is actually the modified version of the scheme in [11], where the second-order extrapolation is pre-estimated by the solutions of the first-order scheme. However, for the anisotropic case, the predictor–corrector scheme is not provably energy stable as well. Hence, in summary, to the best of the author's knowledge, no numerical schemes can be claimed to be provably unconditionally energy stable, fast (e.g., non-iterative), and second-order accurate in time.

In this paper, the main purpose is to develop efficient algorithms that can possess the three desired properties mentioned above to solve the anisotropic Cahn–Hilliard model. To this end, by combining the newly developed SAV approach (cf. [14]) with the stabilization technique, we arrive at a novel stabilized-SAV (SSAV) method. More precisely, we first transform the total free energy integral into a quadratic function of a new, scalar auxiliary variable via a change of variables. Then, for the reformulated model in terms of the new variable, we treat all nonlinear terms in a semi-explicit way. Due to the specialty of the new variable that is non-local type formally, one only needs to solve several decoupled, linear equations with constant coefficients at each time step. Thus the scheme is very easy to implement and fast. Most importantly, some extra linear stabilization terms, which are shown to be crucial to remove oscillations caused by the anisotropic coefficient efficiently, are added to enhance the stability while keeping the required accuracy. We further show that the developed SSAV schemes are unconditional energy stable rigorously, and present various numerical examples to demonstrate the accuracy and stability. To the best of the author's knowledge, the schemes developed in this paper are the first provable unconditionally energy stable schemes with non-iterative computations and second-order accuracy in time for the anisotropic Cahn–Hilliard system.

The rest of the paper is organized as follows. In Section 2, we give a brief introduction of the governing PDE system for the anisotropic Cahn–Hilliard model. In Section 3, we develop two numerical schemes with second-order accuracy for simulating the model, and rigorously prove their unconditional energy stabilities. Various 2D and 3D numerical experiments are given in Section 4 to demonstrate the accuracy and efficiency of the proposed numerical schemes. Finally, some concluding remarks are given in Section 5.

2. Model equations and its energy law

Now we give a brief description for the anisotropic Cahn–Hilliard model [1,2]. Let Ω be a smooth, open, bounded, connected domain in $\mathbb{R}^d$, $d = 2, 3$. Let ϕ be an order parameter which takes the values ± 1 in the two phases with a smooth transitional layer of thickness ϵ. We consider the total free energy as follows,

$$E(\phi) = \int_\Omega \left(\gamma(\boldsymbol{n}) \left(\frac{1}{2}|\nabla\phi|^2 + \frac{1}{\epsilon^2} F(\phi) \right) + \frac{\beta}{2} G(\phi) \right) d\boldsymbol{x}, \tag{2.1}$$

where $\gamma(\boldsymbol{n})$ is a function describing the anisotropic property, and $\boldsymbol{n}$ is the interface normal that is defined as $\boldsymbol{n} = \frac{\nabla\phi}{|\nabla\phi|}$. For 2D, it reads as

$$\boldsymbol{n} = (n_1, n_2)^T = \frac{1}{\sqrt{\phi_x^2 + \phi_y^2}}(\phi_x, \phi_y)^T, \tag{2.2}$$

and for 3D, it reads as

$$\boldsymbol{n} = (n_1, n_2, n_3)^T = \frac{1}{\sqrt{\phi_x^2 + \phi_y^2 + \phi_z^2}}(\phi_x, \phi_y, \phi_z)^T. \tag{2.3}$$

The nonlinear function $F(\phi)$ takes the usual Ginzburg–Landau double-well potential that reads as

$$F(\phi) = \frac{1}{4}(\phi^2 - 1)^2. \tag{2.4}$$

The anisotropic function may take the fourfold form that reads as

$$\gamma(\boldsymbol{n}) = 1 + \alpha\cos(4\Theta) = 1 + \alpha(4\sum_{i=1}^{d} n_i^4 - 3), \tag{2.5}$$

where Θ denotes the orientation angle of the interfacial normal to the interface. The non-negative parameter α in (2.5) describes the intensity of anisotropy. In [1,2], it was indicated that a sufficient big α would produce a strongly anisotropic system, i.e., the underlying Cahn–Hilliard equation is ill-posed. Thus an extra potential $G(\phi)$ is usually added to penalize infinite curvatures in the resulting corners in order to regularize the system, and $\beta > 0$ is the magnitude of the regularization parameter. Two kinds of regularization terms are generally considered where one is the linear regularization based on the bi-Laplacian of the phase variable, that reads as

$$G(\phi) = (\Delta\phi)^2, \tag{2.6}$$

and the other is the nonlinear Willmore regularization that reads as

$$G(\phi) = (\Delta\phi - \frac{1}{\epsilon^2}f(\phi))^2, \tag{2.7}$$

where $f(\phi) = F'(\phi) = \phi(\phi^2 - 1)$. When $\alpha = \beta = 0$, the system degenerates to the isotropic Cahn–Hilliard model.

By taking the H^{-1} gradient flow on the total free energy $E(\phi)$, we obtain the anisotropic Cahn–Hilliard system with the linear regularization:

$$\phi_t = \nabla\cdot(M(\phi)\nabla\mu), \tag{2.8}$$

$$\mu = \frac{1}{\epsilon^2}\gamma(\boldsymbol{n})f(\phi) - \nabla\cdot\mathbf{m} + \beta\Delta^2\phi; \tag{2.9}$$

or with the Willmore regularization:

$$\phi_t = \nabla\cdot(M(\phi)\nabla\mu), \tag{2.10}$$

$$\mu = \frac{1}{\epsilon^2}\gamma(\boldsymbol{n})f(\phi) - \nabla\cdot\mathbf{m} + \beta(\Delta - \frac{1}{\epsilon^2}f'(\phi))(\Delta\phi - \frac{1}{\epsilon^2}f(\phi)), \tag{2.11}$$

where $f'(\phi) = 3\phi^2 - 1$, $M(\phi) \geq M_0 > 0$ is the mobility function that depends on the phase variable ϕ or a constant. The vector field $\mathbf{m}$ is defined as

$$\mathbf{m} = \gamma(\boldsymbol{n})\nabla\phi + \frac{\mathbb{P}\nabla_{\boldsymbol{n}}\gamma(\boldsymbol{n})}{|\nabla\phi|}(\frac{1}{2}|\nabla\phi|^2 + \frac{1}{\epsilon^2}F(\phi)), \tag{2.12}$$

where the matrix $\mathbb{P} = \mathbb{I} - \boldsymbol{n}\boldsymbol{n}^T$.

Without the loss of generality, we adopt the periodic boundary condition to remove all complexities associated with the boundary integrals in this study. We remark that the boundary conditions can also be the no-flux type as

$$\frac{\partial\phi}{\partial\mathbf{n}}\Big|_{\partial\Omega} = \frac{\partial\mu}{\partial\mathbf{n}}\Big|_{\partial\Omega} = \frac{\partial\omega}{\partial\mathbf{n}}\Big|_{\partial\Omega} = 0, \tag{2.13}$$

where $\omega = \Delta\phi$ for linear regularization model and $\omega = \Delta\phi - \frac{1}{\epsilon^2}f(\phi)$ for the Willmore regularization model, $\mathbf{n}$ is the outward normal of the computational domain Ω. All numerical analyses in this paper can be carried out with the no-flux boundary conditions without any further difficulties.

The model equations (2.8)–(2.9) and (2.10)–(2.11) follow the dissipative energy law. By taking the L^2 inner product of (2.8) with $-\mu$, and of (2.9) with ϕ_t, using the integration by parts and combining the obtained two equalities, we obtain

$$\frac{d}{dt}E(\phi) = -\|\sqrt{M(\phi)}\nabla\mu\|^2 \leq 0. \tag{2.14}$$

Meanwhile, the Cahn–Hilliard model conserves the local mass density. By taking the L^2 inner product of (2.8) with 1, one can obtain the mass conservation property directly using integration by parts, that reads as

$$\frac{d}{dt}\int_\Omega \phi d\boldsymbol{x} = 0. \tag{2.15}$$

3. Numerical schemes

We develop in this section a set of linear, second-order, unconditionally energy stable schemes for solving the anisotropic model (2.8)–(2.9) and (2.10)–(2.11). The main challenging issues are to develop suitable approaches to discretize the nonlinear terms, particularly, the terms associated with the anisotropic coefficient $\gamma(\boldsymbol{n})$, as well as the nonlinear term from the Willmore regularization potential (the term associated with β in (2.11)).

For the isotropic Cahn–Hilliard equation where the only numerical challenge is to discretize the nonlinear cubic term $f(\phi)$, there are many successful techniques to preserve the unconditional energy stability, for instances, the convex splitting approach [15], the stabilization approach [13,16–22], Invariant Energy Quadratization method [23–29], and a variety of other type methods, see [7–10], etc. In the convex-splitting method, the convex part of the potential is treated implicitly and the concave part is treated explicitly. This approach is energy stable, however, it usually produces a nonlinear scheme in most cases, thus the implementation is complicated and the computational cost is high. In the stabilization approach, the nonlinear term is treated in a simple explicit way. In order to preserve the energy stability, a linear stabilizing term has to be added, and the magnitude of that term usually depends on the upper bound of the second order derivative of the double-well potential. The stabilization approach introduces a purely linear scheme, thus it is very easy to implement. However, if there does not exist any finite upper bound for that second order derivative, one must make some reasonable revisions to the nonlinear potential in order to obtain a finite bound, for example, a quadratic cut-off function for the double-well potential. Such a method is particularly reliable for those models satisfying the maximum principle. Otherwise, if the maximum principle does not hold, the revisions to the nonlinear potentials may lead to spurious solutions.

Concerning the convex splitting method, it is not clear on whether the nonlinear potentials multiplied with the anisotropic coefficient could be split into the combinations of the convex and concave parts, which exclude the convex splitting approach. With regard to the stabilization approach, it is also not an ideal choice even though there existed some work on this method [11], since (i) it is uncertain whether the PDE solution could satisfy any maximum principle; (ii) the developed scheme is not provable energy stable. Therefore, the ideas of the convex splitting or the stabilization approaches may not be suitable for solving the anisotropic model to obtain the provably energy stable schemes, indeed.

We develop second-order accurate and provably unconditionally energy stable schemes by combining the recently SAV approach [14] with the stabilization technique. Without worrying about whether the continuous/discrete maximum principle holds or a convexity/concavity splitting exists, we arrive at a novel Stabilized-SAV approach. The added linear stabilization terms are particularly efficient in removing oscillations caused by the anisotropic coefficient while keeping the computation fast and easy-to-implement with the required accuracy.

3.1. Linear regularization model

We first deal with the linear regularization model. We define an auxiliary variable $u(t)$ as follows:

$$u(t) = \sqrt{\int_\Omega \gamma(\boldsymbol{n})\big(\frac{1}{2}|\nabla\phi|^2 + \frac{1}{\epsilon^2}F(\phi)\big)d\boldsymbol{x} + B}, \tag{3.1}$$

where B is any constant that ensures the radicand positive (in all numerical examples, we let $B = 1e4$ which is the order of $O(\epsilon^{-2})$. Thus the total free energy (2.1) can be rewritten as

$$E(u,\phi) = u^2 - B + \frac{\beta}{2}\int_\Omega (\Delta\phi)^2 d\boldsymbol{x}, \tag{3.2}$$

Using the new variable u, we then have the following equivalent PDE system,

$$\phi_t = \nabla \cdot (M(\phi)\nabla\mu), \tag{3.3}$$

$$\mu = H(\phi)u + \beta\Delta^2\phi, \tag{3.4}$$

$$u_t = \frac{1}{2}\int_\Omega H(\phi)\phi_t d\boldsymbol{x}, \tag{3.5}$$

where

$$H(\phi) = \frac{\frac{1}{\epsilon^2}\gamma(\boldsymbol{n})f(\phi) - \nabla\cdot\boldsymbol{m}}{\sqrt{\int_\Omega \gamma(\boldsymbol{n})\big(\frac{1}{2}|\nabla\phi|^2 + \frac{1}{\epsilon^2}F(\phi)\big)d\boldsymbol{x} + B}}. \tag{3.6}$$

The transformed system (3.3)–(3.5) forms a closed PDE system with the following initial conditions,

$$\begin{cases} \phi(t=0) = \phi^0, \\ u(t=0) = \sqrt{\int_\Omega \gamma(\boldsymbol{n}^0)\big(\frac{1}{2}|\nabla\phi^0|^2 + \frac{1}{\epsilon^2}F(\phi^0)\big)d\boldsymbol{x} + B}. \end{cases} \tag{3.7}$$

The system (3.3)–(3.5) also follows an energy dissipative laws in terms of the new variable u and ϕ. By taking the L^2 inner product of (3.3) with $-\mu$, of (3.4) with ϕ_t, multiplying (3.5) with $2u$, performing integration by parts and summing all equalities up, we can obtain the energy dissipation law of the new system (3.3)–(3.5) as

$$\frac{d}{dt}E(u,\phi) = -\|\sqrt{M(\phi)}\nabla\mu\|^2 \le 0. \tag{3.8}$$

We note that the new transformed system (3.3)–(3.5) is equivalent to the original system (2.8)–(2.9) for the time continuous case since (3.1) can be easily obtained by integrating (3.5) with respect to the time. Next we will develop unconditionally energy stable linear numerical schemes for time stepping of the transformed system (3.3)–(3.5), and the proposed schemes should formally follow the new energy dissipation law (3.8) in the discrete sense, instead of the energy law for the originated system (2.14).

Let $\delta t > 0$ be a time step size and set $t^n = n\delta t$ for $0 \le n \le N$ with $T = N\delta t$. We also denote the L^2 inner product of any two spatial functions $\phi(\boldsymbol{x})$ and $\psi(\boldsymbol{x})$ by $(\phi,\psi) = \int_\Omega \phi(\boldsymbol{x})\psi(\boldsymbol{x})d\boldsymbol{x}$, and the L^2 norm of the function $\phi(\boldsymbol{x})$ by $\|\phi\|^2 = (\phi,\phi)$. Let ψ^n denote the numerical approximation to $\psi(\cdot,t)|_{t=t^n}$ for any function ψ.

We construct a numerical scheme based on the second-order backward differentiation formula (BDF2).

Scheme 1. *Assuming ϕ^n, u^n and ϕ^{n-1}, u^{n-1} are known, we update ϕ^{n+1}, u^{n+1} by solving*

$$\frac{3\phi^{n+1} - 4\phi^n + \phi^{n-1}}{2\delta t} = \nabla\cdot(M^{*,n+1}\nabla\mu^{n+1}), \tag{3.9}$$

$$\begin{aligned}\mu^{n+1} &= H^{*,n+1}u^{n+1} + \beta\Delta^2\phi^{n+1} \\ &\quad + \frac{S_1}{\epsilon^2}(\phi^{n+1} - 2\phi^n + \phi^{n-1}) - S_2\Delta(\phi^{n+1} - 2\phi^n + \phi^{n-1}),\end{aligned} \tag{3.10}$$

$$3u^{n+1} - 4u^n + u^{n-1} = \frac{1}{2}\int_\Omega H^{*,n+1}(3\phi^{n+1} - 4\phi^n + \phi^{n-1})d\boldsymbol{x}, \tag{3.11}$$

where

$$\phi^{*,n+1} = 2\phi^n - \phi^{n-1},\ \ M^{*,n+1} = M(\phi^{*,n+1}),\ \ H^{*,n+1} = H(\phi^{*,n+1}), \tag{3.12}$$

and S_i with $i = 1,2,3$ are three positive stabilizing parameters.

Remark 3.1. Two second-order linear stabilizers (associated with S_1, S_2) are added in the above scheme. These terms, $\frac{S_1}{\epsilon^2}\Delta(\phi^{n+1} - 2\phi^n + \phi^{n-1})$ and $-S_2\Delta(\phi^{n+1} - 2\phi^n + \phi^{n-1})$ are two commonly used linear stabilizers in the linear stabilization method for solving the isotropic or anisotropic phase field model, (cf.[11] for the anisotropic model, and [16] for the isotropic model). The errors that these two terms introduce are of order $\frac{S_1}{\epsilon^2}\delta t^2\phi_{tt}(\cdot)$ and $S_2\delta t^2\Delta\phi_{tt}(\cdot)$, respectively, which are of the same order as the error introduced by the second-order extrapolation of the nonlinear term $f(\phi)$ and the Laplacian term $\Delta\phi$. Numerical examples show that the combinations of these two stabilizers are crucial to removing all oscillations induced by the anisotropic coefficient $\gamma(\boldsymbol{n})$, since the term $\boldsymbol{n} = \frac{\nabla\phi}{|\nabla\phi|}$ changes its sign frequently as long as when $|\nabla\phi|$ is close to zero (cf. Fig. 4.4 in Section 4).

As far as one can see, we have to solve a nonlocal and coupled system for ϕ^{n+1} and u^{n+1} in the scheme (3.9)–(3.11) at each time step which is very complicated. But in practice, we can simplify the solving process through the following procedure.

We first rewrite (3.11) as follows,

$$u^{n+1} = \frac{1}{2}\int_{\Omega} H^{*,n+1}\phi^{n+1}d\boldsymbol{x} + g^n, \tag{3.13}$$

where

$$g^n = \frac{4u^n - u^{n-1}}{3} - \frac{1}{2}\int_{\Omega} H^{*,n+1}\frac{4\phi^n - \phi^{n-1}}{3}d\boldsymbol{x}.$$

Then the scheme (3.9) can be written as

$$\mathscr{P}(\phi^{n+1}) - \frac{1}{2}\nabla\cdot(M^{*,n+1}\nabla H^{*,n+1})\int_{\Omega} H^{*,n+1}\phi^{n+1}d\boldsymbol{x} = \tilde{g}^n, \tag{3.14}$$

where

$$\begin{cases} \mathscr{P}(\phi) = \dfrac{3}{2\delta t}\phi - \nabla\cdot(M^{*,n+1}\nabla(\beta\Delta^2\phi + \dfrac{S_1}{\epsilon^2}\phi - S_2\Delta\phi)), \\ \tilde{g}^n = \dfrac{4\phi^n - \phi^{n-1}}{2\delta t} + g^n\nabla\cdot(M^{*,n+1}\nabla(H^{*,n+1})) - \nabla\cdot M^{*,n+1}\nabla(\dfrac{S_1}{\epsilon^2}\phi^{*,n+1} - S_2\Delta\phi^{*,n+1}). \end{cases}$$

Define a linear operator $\mathscr{P}^{-1}(\cdot)$, such that for any $\psi \in L^2(\Omega)$, $\phi = \mathscr{P}^{-1}(\psi)$ is defined as

$$\frac{3}{2\delta t}\phi - \nabla\cdot(M^{*,n+1}\nabla(\beta\Delta^2\phi + \frac{S_1}{\epsilon^2}\phi - S_2\Delta\phi)) = \psi. \tag{3.15}$$

By applying the operator $\mathscr{P}^{-1}$ to (3.14), then we obtain

$$\phi^{n+1} - \frac{1}{2}\mathscr{P}^{-1}(\nabla\cdot(M^{*,n+1}\nabla H^{*,n+1}))\int_{\Omega} H^{*,n+1}\phi^{n+1}d\boldsymbol{x} = \mathscr{P}^{-1}(\tilde{g}^n). \tag{3.16}$$

By taking the L^2 inner product with $H^{*,n+1}$, we obtain

$$\int_{\Omega} H^{*,n+1}\phi^{n+1}d\boldsymbol{x} = \frac{\int_{\Omega} H^{*,n+1}\mathscr{P}^{-1}(\tilde{g}^n)d\boldsymbol{x}}{1 - \frac{1}{2}\int_{\Omega} H^{*,n+1}\mathscr{P}^{-1}(\nabla\cdot(M^{*,n+1}\nabla H^{*,n+1}))d\boldsymbol{x}}. \tag{3.17}$$

It is easy to check the term in the denominator $-\int_{\Omega} H^{*,n+1}\mathscr{P}^{-1}(\nabla\cdot(M^{*,n+1}\nabla H^{*,n+1}))d\boldsymbol{x} \geq 0$ since $-\mathscr{P}^{-1}(\nabla\cdot(M^{*,n+1}\nabla(\bullet)))$ is a positive definite operator. Therefore, in the computations, one only needs to find $\psi_1 = \mathscr{P}^{-1}(\tilde{g}^n)$ and $\psi_2 = \mathscr{P}^{-1}(\nabla\cdot(M^{*,n+1}\nabla H^{*,n+1}))$, that means to solve the following two sixth order equations,

$$\frac{3}{2\delta t}\psi_1 - \nabla\cdot(M^{*,n+1}\nabla(\beta\Delta^2\psi_1 + \frac{S_1}{\epsilon^2}\psi_1 - S_2\Delta\psi_1)) = \tilde{g}^n, \tag{3.18}$$

and

$$\frac{3}{2\delta t}\psi_2 - \nabla\cdot(M^{*,n+1}\nabla(\beta\Delta^2\psi_2 + \frac{S_1}{\epsilon^2}\psi_2 - S_2\Delta\psi_2)) = \nabla\cdot(M^{*,n+1}\nabla H^{*,n+1}), \tag{3.19}$$

with the periodic boundary conditions. Once ψ_1 and ψ_2 are obtained, by applying (3.17) to get $\int_{\Omega} H^{*,n+1}\phi^{n+1}d\boldsymbol{x}$, we then solve the third sixth order equation (3.14) to obtain ϕ^{n+1}.

To summarize, the scheme (3.9)–(3.11) can be easily implemented in the following manner:

- Compute ψ_1 and ψ_2 by solving two sixth-order equations, (3.18) and (3.19);
- Compute $\int_{\Omega} H^{*,n+1}\phi^{n+1}d\boldsymbol{x}$ from (3.17) and u^{n+1} from (3.13);
- Compute ϕ^{n+1} by solving the third sixth-order equation (3.14).

Hence, instead of solving nonlocal equations that might need some costly iterative solvers, the total cost of solving scheme (3.9)–(3.11) at each time step is just solving three decoupled, sixth-order linear equations.

Remark 3.2. It is remarkable that, if the mobility function $M(\phi)$ is a constant, e.g., $M(\phi) = M$, then these sixth-order equations form like

$$\frac{3}{2M\delta t}\psi - \frac{S_1}{\epsilon^2}\Delta\psi + S_2\Delta^2\psi - \beta\Delta^3\psi = \cdots. \tag{3.20}$$

These equations with periodic boundary conditions can be easily solved by using the Fourier-spectral methods. Hence, the stabilized SAV scheme is extremely efficient and easy to implement.

Now we prove the scheme (3.9)–(3.11) is unconditionally energy stable as follows.

Theorem 3.1. *The scheme (3.9)–(3.11) is unconditionally energy stable which satisfies the following discrete energy dissipation law,*

$$\frac{1}{\delta t}(E^{n+1}_{linear} - E^{n}_{linear}) \le -\|\sqrt{M^{*,n+1}}\nabla\mu^{n+1}\|^2 \le 0, \tag{3.21}$$

where

$$\begin{aligned} E^{n+1}_{linear} = {} & \frac{(u^{n+1})^2 + (2u^{n+1} - u^n)^2}{2} + \frac{\beta}{2}\Big(\frac{\|\Delta\phi^{n+1}\|^2 + \|2\Delta\phi^{n+1} - \Delta\phi^n\|^2}{2}\Big) \\ & + \frac{S_1}{\epsilon^2}\frac{\|\phi^{n+1} - \phi^n\|^2}{2} + S_2\frac{\|\nabla\phi^{n+1} - \nabla\phi^n\|^2}{2}. \end{aligned} \tag{3.22}$$

Proof. By taking the L^2 inner product of (3.9) with $-2\delta t\mu^{n+1}$, we obtain

$$-(3\phi^{n+1} - 4\phi^n + \phi^{n-1}, \mu^{n+1}) = 2\delta t\|\sqrt{M^{*,n+1}}\nabla\mu^{n+1}\|^2. \tag{3.23}$$

By taking the L^2 inner product of (3.10) with $3\phi^{n+1} - 4\phi^n + \phi^{n-1}$, and using integration by parts, we obtain

$$\begin{aligned} (\mu^{n+1}, 3\phi^{n+1} - 4\phi^n + \phi^{n-1}) = {} & u^{n+1}(H^{*,n+1}, 3\phi^{n+1} - 4\phi^n + \phi^{n-1}) \\ & + \frac{S_1}{\epsilon^2}(\phi^{n+1} - 2\phi^n + \phi^{n-1}, 3\phi^{n+1} - 4\phi^n + \phi^{n-1}) \\ & + S_2(\nabla(\phi^{n+1} - 2\phi^n + \phi^{n-1}), \nabla(3\phi^{n+1} - 4\phi^n + \phi^{n-1})) \\ & + \beta(\Delta\phi^{n+1}, \Delta(3\phi^{n+1} - 4\phi^n + \phi^{n-1}). \end{aligned} \tag{3.24}$$

By multiplying (3.11) with $-2u^{n+1}$, we obtain

$$-2(3u^{n+1} - 4u^n + u^{n-1})u^{n+1} = -u^{n+1}\int_\Omega H^{*,n+1}(3\phi^{n+1} - 4\phi^n + \phi^{n-1})d\boldsymbol{x}. \tag{3.25}$$

Combining the above equations and applying the following two identities

$$\begin{aligned} & 2a(3a - 4b + c) = a^2 + (2a - b)^2 - b^2 - (2b - c)^2 + (a - 2b + c)^2, \\ & (3a - 4b + c)(a - 2b + c) = (a - b)^2 - (b - c)^2 + 2(a - 2b + c)^2, \end{aligned} \tag{3.26}$$

we obtain

$$\begin{aligned} & \Big((u^{n+1})^2 + (2u^{n+1} - u^n)^2\Big) - \Big((u^n)^2 + (2u^n - u^{n-1})^2\Big) \\ & + \frac{\beta}{2}\Big(\|\Delta\phi^{n+1}\|^2 + \|2\Delta\phi^{n+1} - \Delta\phi^n\|^2\Big) - \frac{\beta}{2}\Big(\|\Delta\phi^n\|^2 + \|2\Delta\phi^n - \Delta\phi^{n-1}\|^2\Big) \\ & + \frac{S_1}{\epsilon^2}\|\phi^{n+1} - \phi^n\|^2 - \frac{S_1}{\epsilon^2}\|\phi^n - \phi^{n-1}\|^2 \\ & + S_2\|\nabla\phi^{n+1} - \nabla\phi^n\|^2 - S_2\|\nabla\phi^n - \nabla\phi^{n-1}\|^2 \\ & + (u^{n+1} - 2u^n + u^{n-1})^2 + \frac{2S_1}{\epsilon^2}\|\phi^{n+1} - 2\phi^n + \phi^{n-1}\|^2 \end{aligned}$$

$$+ 2S_2\|\nabla(\phi^{n+1} - 2\phi^n + \phi^{n-1})\|^2 + \frac{\beta}{2}\|\Delta(\phi^{n+1} - 2\phi^n + \phi^{n-1})\|^2$$
$$= -2\delta t\|\sqrt{M^{*,n+1}}\nabla\mu^{n+1}\|^2.$$

Finally, we obtain the desired result after dropping some positive terms. □

Remark 3.3. Heuristically, $\frac{1}{\delta t}(E^{n+1}_{linear} - E^n_{linear})$ is a second-order approximation of $\frac{d}{dt}\mathcal{E}(\phi, u)$ at $t = t^{n+1}$. For any smooth variable ψ with time, we have

$$\frac{\|\psi^{n+1}\|^2 - \|2\psi^{n+1} - \psi^n\|^2}{2\delta t} - \frac{\|\psi^n\|^2 - \|2\psi^n - \psi^{n-1}\|^2}{2\delta t}$$
$$\cong \frac{\|\psi^{n+2}\|^2 - \|\psi^n\|^2}{2\delta t} + O(\delta t^2) \cong \frac{d}{dt}\|\psi(t^{n+1})\|^2 + O(\delta t^2), \tag{3.27}$$

and

$$\frac{\|\psi^{n+1} - \psi^n\|^2 - \|\psi^n - \psi^{n-1}\|^2}{2\delta t} \cong O(\delta t^2). \tag{3.28}$$

Remark 3.4. It is also straightforward to develop the second-order Crank–Nicolson scheme where the linear stabilizers terms still form like $\psi^{n+1} - 2\psi^n + \psi^{n-1}$. We omit the details to the interested readers since the proof of energy stability is quite similar to Theorem 3.1. In addition, although we consider only time discrete schemes in this study, the results can be carried over to any consistent finite-dimensional Galerkin approximations in the space since the proofs are all based on a variational formulation with all test functions in the same space as the space of the trial functions.

3.2. Willmore regularization model

We deal with the Willmore regularization model in this subsection. Similar to the linear regularization case, we define an auxiliary variable as follows:

$$u(t) = \sqrt{\int_\Omega \Big(\gamma(\boldsymbol{n})\big(\frac{1}{2}|\nabla\phi|^2 + \frac{1}{\epsilon^2}F(\phi)\big) + \frac{\beta}{2}(\Delta\phi - \frac{1}{\epsilon^2}f(\phi))^2\Big)d\boldsymbol{x} + B}, \tag{3.29}$$

where B is a constant to ensure the radicand positive and we let $B \sim O(\epsilon^{-2})$ in computations. Thus the total free energy (2.1) can be rewritten as

$$E(u, \phi) = u^2 - B. \tag{3.30}$$

Using these new variables u, we then have the following equivalent PDE system,

$$\phi_t = \nabla\cdot(M(\phi)\nabla\mu), \tag{3.31}$$
$$\mu = Z(\phi)u, \tag{3.32}$$
$$u_t = \frac{1}{2}\int_\Omega Z(\phi)\phi_t d\boldsymbol{x}, \tag{3.33}$$

where

$$Z(\phi) = \frac{\frac{1}{\epsilon^2}\gamma(\boldsymbol{n})f(\phi) - \nabla\cdot\boldsymbol{m} + \beta(\Delta - \frac{1}{\epsilon^2}f'(\phi))(\Delta\phi - \frac{1}{\epsilon^2}f(\phi))}{\sqrt{\int_\Omega\Big(\gamma(\boldsymbol{n})\big(\frac{1}{2}|\nabla\phi|^2 + \frac{1}{\epsilon^2}F(\phi)\big) + \frac{\beta}{2}(\Delta\phi - \frac{1}{\epsilon^2}f(\phi))^2\Big)d\boldsymbol{x} + B}}. \tag{3.34}$$

The system (3.31)–(3.33) is equipped with the following initial conditions,

$$\begin{cases}\phi(t=0) = \phi^0,\\ u(t=0) = \sqrt{\int_\Omega\Big(\gamma(\boldsymbol{n}^0)\big(\frac{1}{2}|\nabla\phi^0|^2 + \frac{1}{\epsilon^2}F(\phi^0)\big) + \frac{\beta}{2}(\Delta\phi^0 - \frac{1}{\epsilon^2}f(\phi^0))^2\Big)d\boldsymbol{x} + B}.\end{cases} \tag{3.35}$$

It is easy to see that the system (3.31)–(3.33) follows an energy dissipative law in terms of the new variable u and ϕ. By taking the L^2 inner product of (3.3) with $-\mu$, of (3.4) with ϕ_t, multiplying (3.5) with $2u$, performing integration by parts, and summing all equalities up, we can obtain the energy dissipation law of the new system (3.3)–(3.5) as

$$\frac{d}{dt}E(u,\phi) = -\|\sqrt{M(\phi)}\nabla\mu\|^2 \le 0. \tag{3.36}$$

We present the second-order numerical scheme based on the BDF2 for solving the transformed model (3.31)–(3.33).

Scheme 2. *Assuming ϕ^n, u^n and ϕ^{n-1}, u^{n-1} are known, we update ϕ^{n+1}, u^{n+1} by solving*

$$\frac{3\phi^{n+1}-4\phi^n+\phi^{n-1}}{2\delta t} = \nabla\cdot(M^{*,n+1}\nabla\mu^{n+1}), \tag{3.37}$$

$$\begin{aligned}\mu^{n+1} = {} & Z^{*,n+1}u^{n+1} + \frac{S_1}{\epsilon^2}(\phi^{n+1}-2\phi^n+\phi^{n-1}) \\ & -S_2\Delta(\phi^{n+1}-2\phi^n+\phi^{n-1}) + S_3\Delta^2(\phi^{n+1}-2\phi^n+\phi^{n-1}),\end{aligned} \tag{3.38}$$

$$3u^{n+1}-4u^n+u^{n-1} = \frac{1}{2}\int_\Omega Z^{*,n+1}(3\phi^{n+1}-4\phi^n+\phi^{n-1})d\boldsymbol{x}, \tag{3.39}$$

where $Z^{*,n+1} = Z(\phi^{*,n+1})$, $S_{i,i=1,2,3}$ are three positive stabilizing parameters.

Here we add the third stabilization term associated with S_3 is of the order $S_3\delta t^2\Delta^2\phi_{tt}(\cdot)$ since we also treat the Willmore regularization term in the semi-explicit way. Thus we choose $S_3 \sim O(\beta)$ in practice.

Since the scheme (3.37)–(3.39) is almost identical to the scheme (3.9)–(3.11) formally, thus we omit the details of its implementation procedure and only present the theorem of energy stability as follows.

Theorem 3.2. *The scheme (3.37)–(3.39) is unconditionally energy stable which satisfies the following discrete energy dissipation law,*

$$\frac{1}{\delta t}(E^{n+1}_{will} - E^n_{will}) \le -\|\sqrt{M^{*,n+1}}\nabla\mu^{n+1}\|^2 \le 0, \tag{3.40}$$

where

$$\begin{aligned}E^{n+1}_{will} = {} & \frac{(u^{n+1})^2+(2u^{n+1}-u^n)^2}{2} + \frac{S_1}{\epsilon^2}\frac{\|\phi^{n+1}-\phi^n\|^2}{2} \\ & + S_2\frac{\|\nabla\phi^{n+1}-\nabla\phi^n\|^2}{2} + S_3\frac{\|\Delta\phi^{n+1}-\Delta\phi^n\|^2}{2}.\end{aligned} \tag{3.41}$$

4. Numerical simulations

We now present various numerical examples to demonstrate the accuracy, energy stability, and efficiency of the developed schemes. Here, we set the computational domain as $\Omega = [0, 2\pi]^d$, $d = 2, 3$ and use periodic boundary conditions. The Fourier-spectral method is adopted to discretize the space, where 129^2 Fourier modes are used for 2D simulations, and 129^3 Fourier modes are used for 3D simulations.

If not explicitly specified, the default values of order parameters and stabilization parameters are set as follows,

$$M(\phi) = 1, \epsilon = 6\text{e–}2, \alpha = 0.3, \beta = 6\text{e–}4, S_1 = 4, S_2 = 4, S_3 = 1\text{e–}3. \tag{4.1}$$

4.1. Accuracy test

We first perform numerical simulations to test the convergence rates of the two proposed schemes, the stabilized SAV scheme (3.9)–(3.11) for the linear regularization model, denoted by SSAV; and the stabilized SAV scheme (3.37)–(3.39) for the Willmore regularization model, denoted by SSAV-W. For comparisons, we also compute the convergence rates for the two non-stabilized schemes, namely, the scheme (3.9)–(3.11) with $S_1 = S_2 = 0$, denoted by SAV; and the scheme (3.37)–(3.39) with $S_1 = S_2 = S_3 = 0$, denoted by SAV-W.

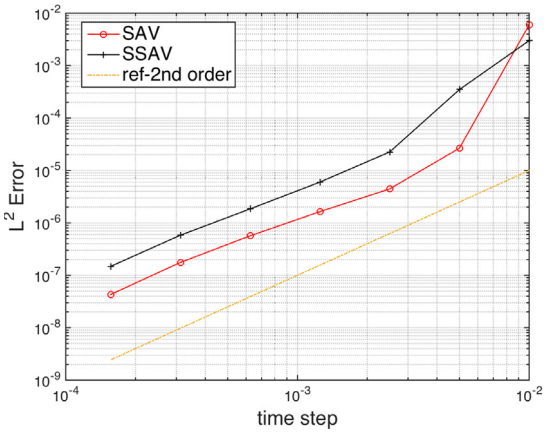

(a) SSAV and SAV (isotropic) with $M = 0.001$.

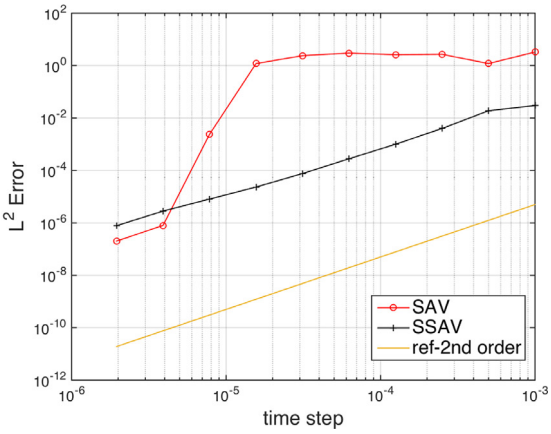

(b) SSAV and SAV (isotropic) with $M = 1$.

Fig. 4.1. The L^2 numerical errors of ϕ computed by using the stabilized scheme SSAV and non-stabilized scheme SAV with various time steps for the isotropic Cahn–Hilliard model ($\gamma(\boldsymbol{n}) = 1, \beta = 0$) with two different mobility parameters where (a) $M = 0.001$ and (b) $M = 1$. Other parameters are from (4.1).

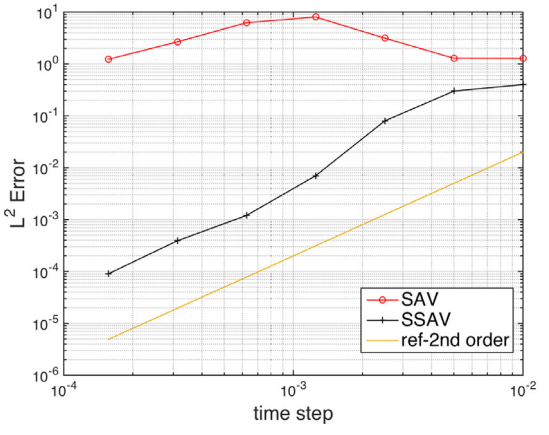

(a) SSAV and SAV (anisotropic).

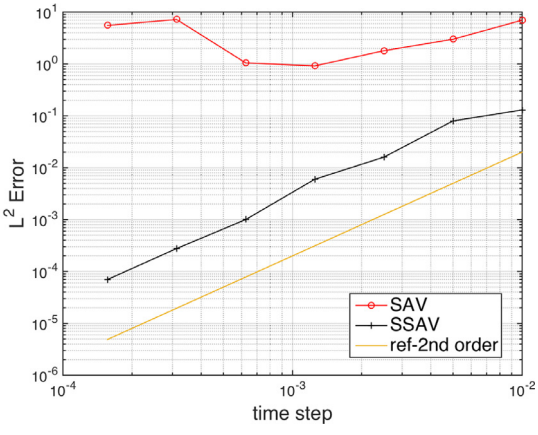

(b) SSAV-W and SAV-W (anisotropic).

Fig. 4.2. (a) The L^2 numerical errors of ϕ that are computed using the stabilized scheme SSAV and the non-stabilized scheme SAV with various time steps for the anisotropic Cahn–Hilliard model with linear regularization. (b) The L^2 numerical errors of ϕ computed by using the stabilized scheme SSAV-W and the non-stabilized scheme SAV-W with various time steps for the anisotropic Cahn–Hilliard model with Willmore regularizations. For both figures, the mobility parameter $M = 1$, anisotropic strength $\alpha = 0.1$, and other parameters are from (4.1).

We set the initial conditions as follows,

$$\phi(x, y, t = 0) = \sum_{i=1}^{2} -\tanh\left(\frac{\sqrt{(x - x_i)^2 + (y - y_i)^2} - r_i}{1.2\epsilon}\right) + 1, \tag{4.2}$$

where $(x_1, y_1, r_1) = (\pi - 0.7, \pi - 0.6, 1.5)$ and $(x_2, y_2, r_2) = (\pi + 1.65, \pi + 1.6, 0.7)$. Since the exact solutions are not known, we choose the solution obtained with the time step size $\delta t = 1\text{e}{-7}$ computed by the scheme SSAV and SSAV-W as the benchmark solution (approximately the exact solution) for computing errors of each model.

We first test the convergences of schemes SSAV and SAV for the isotropic Cahn–Hilliard model ($\gamma(\boldsymbol{n}) = 1, \beta = 0$) by varying two mobility parameters of $M = 0.001$ and $M = 1$ and using other parameters from (4.1). A special remark is, for the isotropic model, we treat the $\Delta\phi$ implicitly and define the auxiliary variable

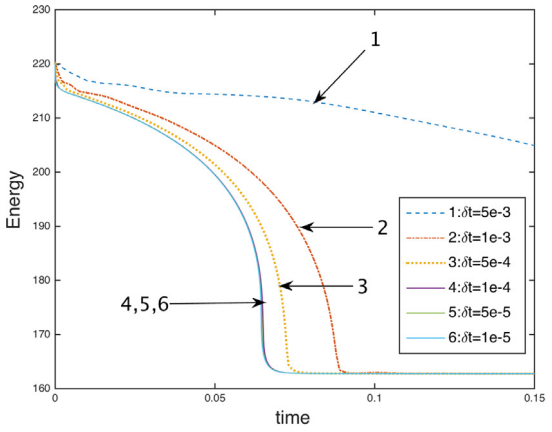

(a) Energy evolution with various time steps.

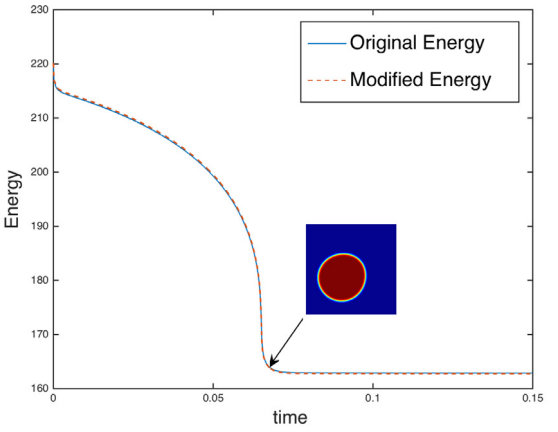

(b) Evolutions of (2.1) and (3.2) with $\delta t = 1\text{e}{-4}$.

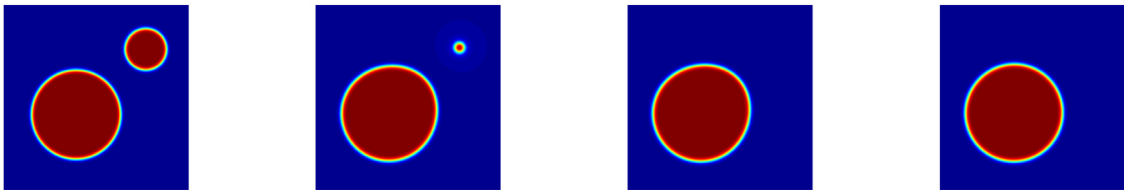

(c) snapshots of the phase variable ϕ.

Fig. 4.3. Coarsening dynamics of two 2D circles for the isotropic Cahn–Hilliard model with $\alpha = 1, \beta = 0$. (a) Time evolution of the total free energy functional (2.1) computed by using six different time steps. (b) Time evolution of the free energy (2.1) and the modified energy (3.2) computed by using $\delta t = 1\text{e}{-4}$. (c) The 2D dynamical evolution of the phase variable ϕ by using $\delta t = 1\text{e}{-4}$ where snapshots are taken at $t = 0$, 6.36e–2, 7e–3, and 1.5e–1.

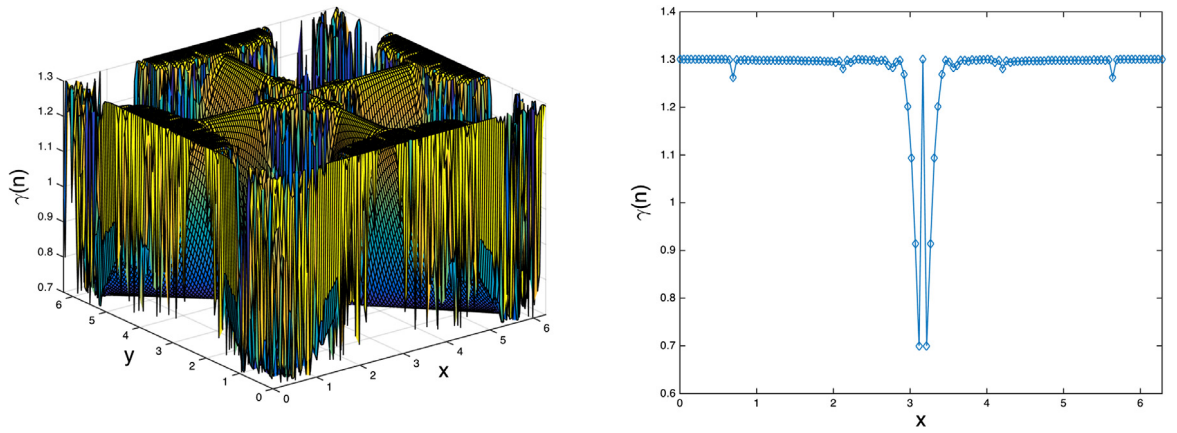

Fig. 4.4. The profile of $\gamma(\boldsymbol{n}^0)$ with $\alpha = 0.3$ by using the initial condition (4.3). The left subfigure is the 2D surface plots of $\gamma(\boldsymbol{n}^0)$, and the right subfigure is the 1D cross-section of $\gamma(\boldsymbol{n}_0)|_{(\cdot, y=\pi)}$.

$u(t) = \sqrt{\int_\Omega \frac{1}{\epsilon^2} F(\phi) d\boldsymbol{x} + B}$. Thus in the stabilized scheme SSAV for solving the isotropic model, the second stabilizer is not needed, namely, we set $S_1 = 4$, $S_2 = 0$.

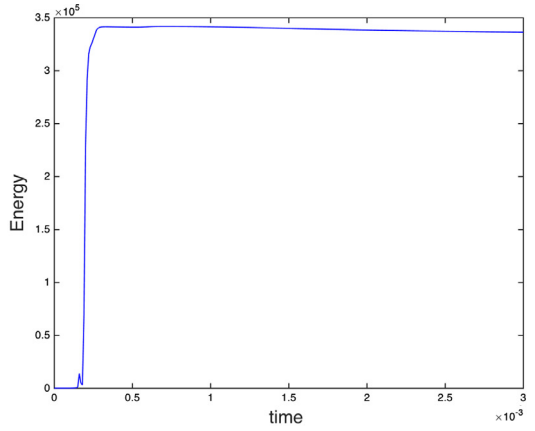

(a) $\delta t = 1\text{e}{-5}$.

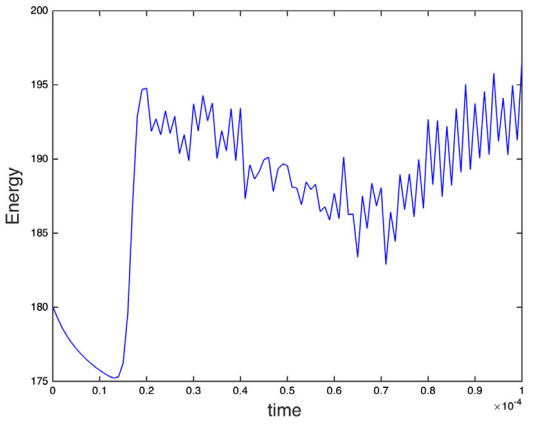

(b) $\delta t = 1\text{e}{-6}$.

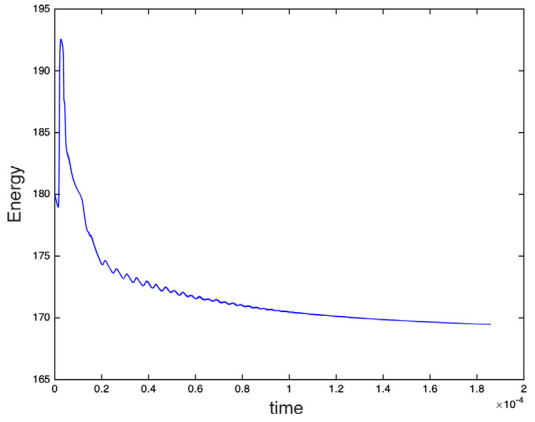

(c) $\delta t = 1\text{e}{-7}$.

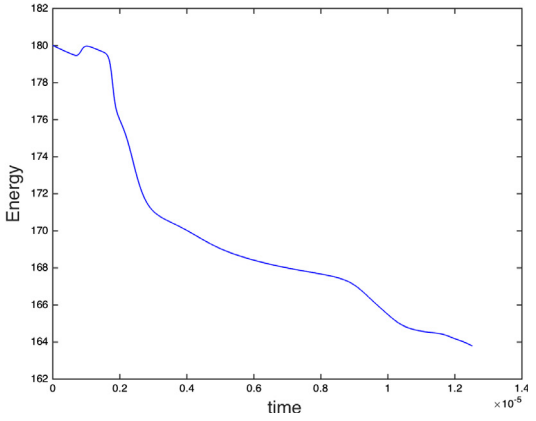

(d) $\delta t = 1\text{e}{-8}$.

Fig. 4.5. Time evolution of the total free energy functional (2.1) for the anisotropic linear regularization model by using the non-stabilized scheme SAV for four time steps of 1e–5, 1e–6, 1e–7, and 1e–8.

We perform the refinement test for the temporal convergence and present the L^2 errors of ϕ between the numerical solution with various time steps and the benchmark solution at $t = 0.1$ in Fig. 4.1. Some remarkable features observed from Fig. 4.1 are listed as follows.

- When $M = 0.001$, both schemes, SSAV and SAV, present the second-order convergence rate asymptotically, and good approximations to the exact solution, regardless of whether they are stabilized or not, shown in Fig. 4.1(a). But obviously, the magnitude of errors computed by the SSAV is bigger than that computed by the SAV since extra splitting errors are induced by the two added stabilizers.
- When $M = 1$, both schemes, SSAV and SAV, are still stable for all tested time steps, shown in Fig. 4.1(b). However, the non-stabilized scheme SAV shows very bad accuracy results for $\delta t > 3.90625\text{e}{-6}$. When $\delta t \leq 3.90625\text{e}{-6}$, it presents good approximations to the exact solution and second-order convergence rate. On the contrary, the stabilized scheme SSAV is not only stable for all tested time steps but also presents good approximations to the exact solutions and show second-order accuracy all along. But when $\delta t \leq 3.90625\text{e}{-6}$, the magnitude of errors computed by the stabilized scheme SSAV is remarkably bigger than that computed by the non-stabilized scheme SAV due to extra splitting errors introduced by stabilization terms.

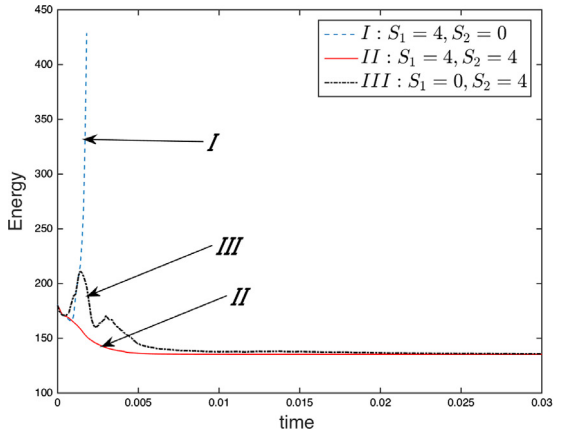

(a) Energy evolutions with three combinations of stabilizers using the stabilized scheme SSAV.

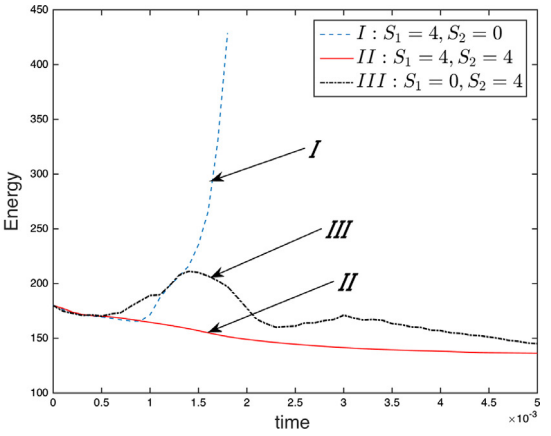

(b) A close-up view.

Fig. 4.6. Time evolution of the free energy functional (2.1) of three combinations of linear stabilizers, for solving the anisotropic linear regularization model with the initial condition of (4.3) by using the stabilized scheme SSAV and time step δt = 1e–4. The left subfigure (a) is the energy profile for $t \in [0, 3e{-}2]$, and the right subfigure (b) is a close-up view for $t \in [0, 5e{-}3]$.

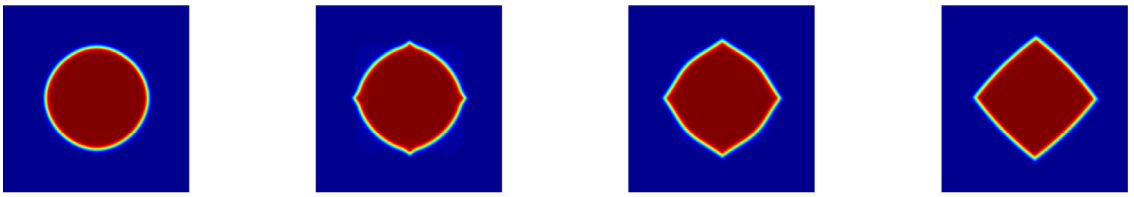

(a) Snapshots of ϕ.

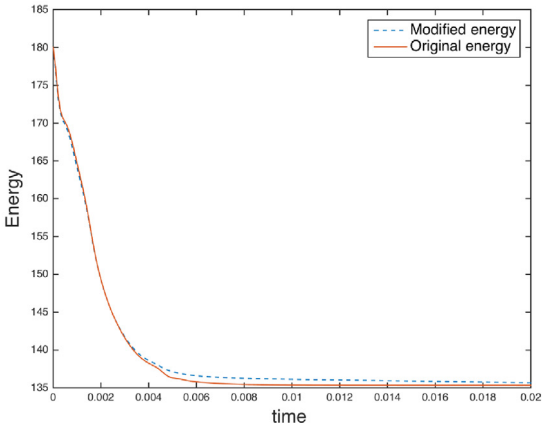

(b) Energy evolutions with time.

Fig. 4.7. (a) The 2D dynamical evolution of the phase variable ϕ for the anisotropic linear regularization model by using the initial condition (4.3) and the stabilized scheme SSAV. Snapshots of the numerical approximation are taken at t = 5e–4, 1.5e–3, 2.5e–3, and 2e–2. (b) Time evolution of the two free energy functionals, the original energy (2.1) and the modified energy (3.2).

Next, we set $M = 1$ and perform the mesh refinement test for the anisotropic Cahn–Hilliard models with the linear and Willmore regularizations where the anisotropic strength is $\alpha = 0.1$ and all other parameters are from

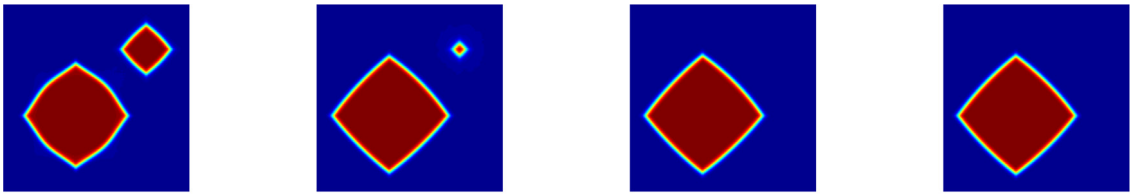

(a) Snapshots of ϕ.

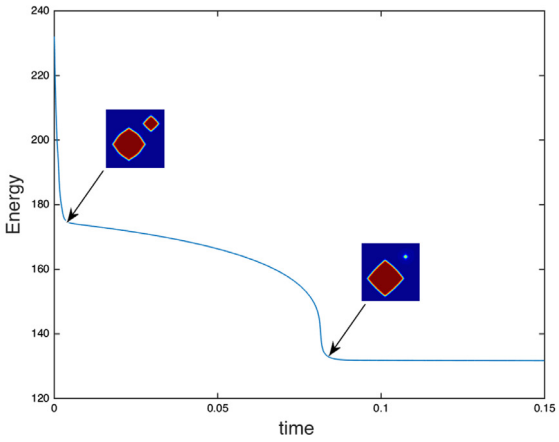

(b) Evolutions of the total free energy.

Fig. 4.8. (a) The 2D dynamical evolution of the phase variable ϕ for the anisotropic model with the linear regularization, where the initial condition is (4.2) and snapshots are taken at $t =$ 2e–3, 9.2e–2, 1e–1, and 2e–1. (b) Time evolution of the total free energy functional (2.1).

(4.1). We use the same initial condition of (4.2), and choose the solution computed by the scheme SSAV with the time step size $\delta t =$ 1e–7 as the benchmark solution. The L^2 errors of the phase variable between the numerical solution and the exact solution at $t = 0.1$ with different time step sizes are shown in Fig. 4.2. It is found that the performance of these four schemes, SSAV and SAV, SSAV-W and SAV-W, is similar to Fig. 4.1(b), where we observe that (i) even though the two non-stabilized schemes, SAV and SAV-W, are stable for all tested time steps, they show very bad accuracy results, (ii) with the stabilizers, the two stabilized schemes, SSAV and SSAV-W, are stable for all tested time steps and perform good approximations and second-order accuracy all along.

In summary, through these accuracy tests, we conclude

- For the isotropic Cahn–Hilliard model with a low mobility parameter, the stabilizers are not needed. The non-stabilized scheme SAV is already very stable and can show very good approximations to the exact solutions and second-order convergence rate.
- For the isotropic Cahn–Hilliard model with a high mobility parameter, (i) when larger time steps are used, the stabilized scheme SSAV can overwhelmingly defeat their non-stabilized version SAV, for both accuracy and stability; (ii) when very tiny time steps are used, the non-stabilized scheme SAV is superior to its stabilized version SSAV concerning the accuracy.
- For the anisotropic Cahn–Hilliard model, the stabilized schemes (SSAV and SSAV-W) can overwhelmingly defeat their non-stabilized versions (SAV and SAV-W), for both accuracy and stability.

4.2. Isotropic evolution for two 2D circles

In this example, by setting $M(\phi) = 1$, we investigate how the coarsening effect acts for two 2D circles by solving the isotropic Cahn–Hilliard model using the scheme SSAV with the initial condition of (4.2) where $\gamma(\boldsymbol{n}) = 1$, $\beta = 0$, and other parameters are from (4.1).

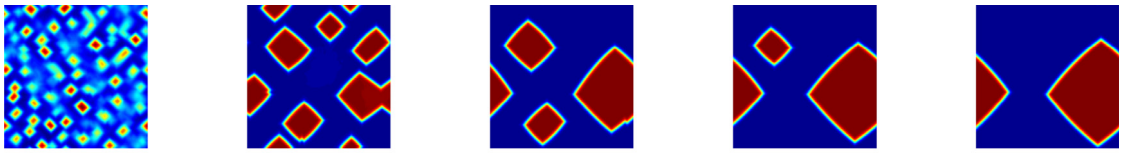

(a) Snapshots of ϕ.

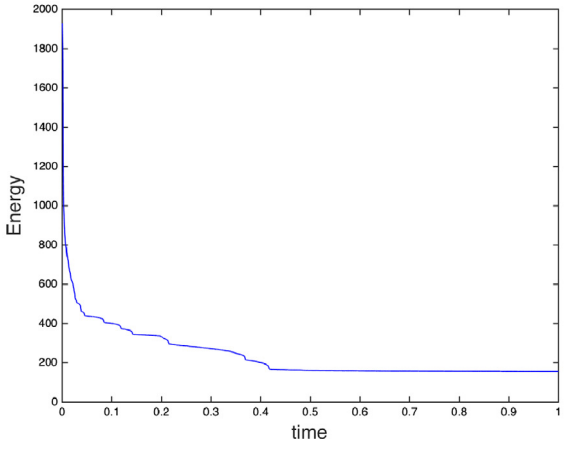

(b) Evolutions of the total free energy.

Fig. 4.9. (a) 2D dynamical evolutions of ϕ for the spinodal decomposition example for solving the anisotropic linear regularization model, where the initial condition is (4.4) and snapshots are taken at t = 1.5e–3, 1e–2, 2.5e–1, 5e–1, and 1. (b) Time evolution of the total free energy functional (2.1).

We first estimate the rough range of the allowable maximum time step size in order to obtain good accuracy and to consume as low computational cost as possible. This time step range could be obtained through comparing the energy evolution curve plots with various time steps, shown in Fig. 4.3(a), where we compare the time evolution of the free energy for six different time step sizes until the equilibrium. We observe that all energy curves decay monotonically for all time step sizes, which numerically confirms that our algorithms are unconditionally energy stable. For smaller time steps of 1e–5, 5e–5, and 1e–4, the three energy curves coincide very well. But for the larger time step of 5e–4, 1e–3, and 5e–3, the energy curves deviate visibly away from others. This means the adopted time step size should not be larger than 1e–4, in order to get reasonably good accuracy.

In Fig. 4.3(b), we present the evolution of the two free energy functionals, the modified energy (3.2) and original energy (2.1) computed using δt = 1e–4. We cannot tell any quantitative differences between these two energies and both decay to the equilibrium, monotonically. At around t = 6.36e–2, the energies undergo a rapid decrease when the complete absorption happens, and the system achieves the equilibrium of circular shape right after that. In Fig. 4.3(c), snapshots of ϕ at various moments are presented, where we observe the coarsening effect that the small circle is absorbed into the big circle.

4.3. Anisotropic model with linear regularizations

In this subsection, we perform simulations for the anisotropic system with linear regularizations. We use parameters from (4.1), if not explicitly specified.

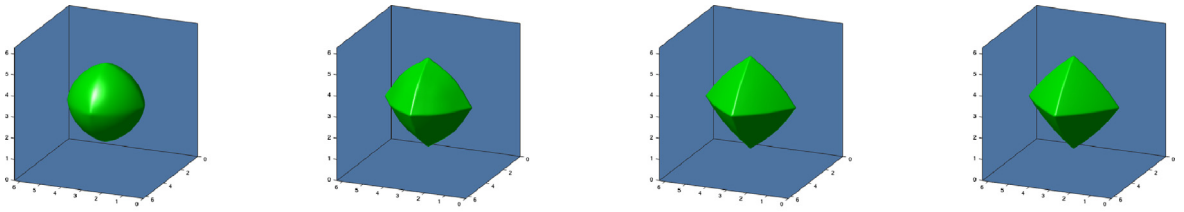

(a) Snaphots of the isosurfaces of ϕ.

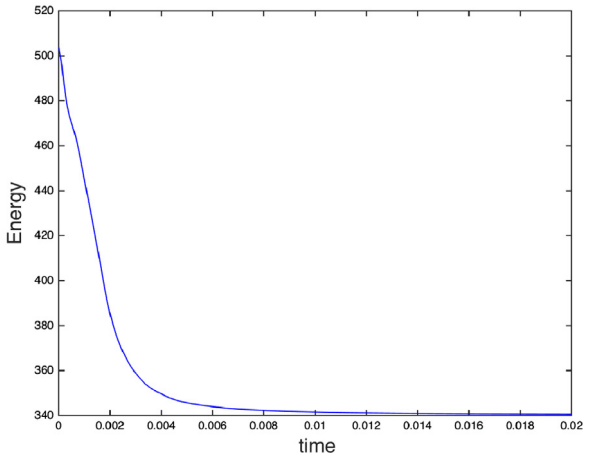

(b) Evolutions for the total free energy.

Fig. 4.10. (a) The dynamical evolution of a 3D sphere for the anisotropic linear regularization model by using the initial condition (4.5) where snapshots of the isosurfaces of the phase field variable $\{\phi = 0\}$ are taken at t = 1.2e–3, 3e–3, 6e–3 and 2e–1. (b) Time evolution of the total free energy functional (2.1).

4.3.1. Anisotropic evolution of a 2D circle

We first perform the simulation for the evolution of a 2D circle where the initial condition is specified as follows

$$\phi(x, y, t = 0) = -\tanh\Big(\frac{\sqrt{(x-\pi)^2 + (y-\pi)^2} - 1.7}{2\epsilon}\Big). \tag{4.3}$$

In Fig. 4.4, we present the 2D profile of $\gamma(\boldsymbol{n}_0)$ and 1D cross-section of $\gamma(\boldsymbol{n}_0)|_{(\cdot, y=\pi)}$, where we observe that a high oscillation profile appears almost everywhere in the computed domain.

We first examine whether the non-stabilized scheme SAV is effective for solving the anisotropic model. In Fig. 4.5, we present the time evolutions of the free energy (2.1) by using four time steps δt = 1e–5, 1e–6, 1e–7, and 1e–8. We observe that the free energy either increases or oscillates even when very tiny time steps are used, that implies the non-stabilized scheme SAV meets the bottleneck for handling the anisotropic model.

Thus we solve the anisotropic model by using the stabilized scheme SSAV. By using the same time step δt = 1e–4 as the previous isotropic example, we test performance of three combinations of stabilizers: (I) $S_1 = 4$, $S_2 = 0$, (II) $S_1 = 4$, $S_2 = 4$ (default values from (4.1)), and (III) $S_1 = 0$, $S_2 = 4$. In Fig. 4.6, the evolutions of the free energy functional (2.1) are shown for these three cases. For (I) and (III), the energies either present some non-physical oscillations or increase with time. These unreasonable phenomena can be eliminated efficiently for combination (II), that means the values in (II) can suppress high-frequency oscillations efficiently.

In Fig. 4.7(a), with the stabilizer (II) and time step δt = 1e–4, we show the dynamics of how a 2D circular shape interface with full orientations evolves to an anisotropic pyramid with missing orientations at four corners.

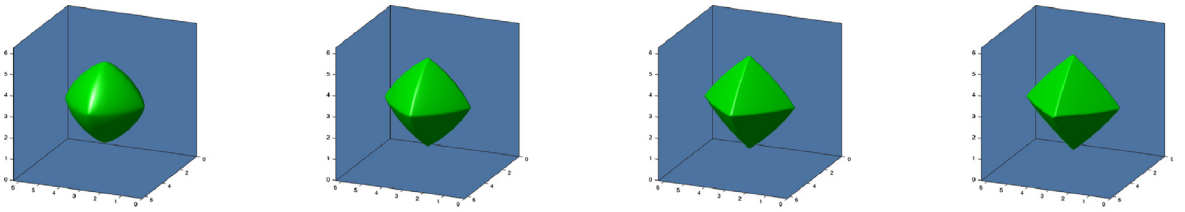

(a) Isosurfaces of equilibrium solution for various α.

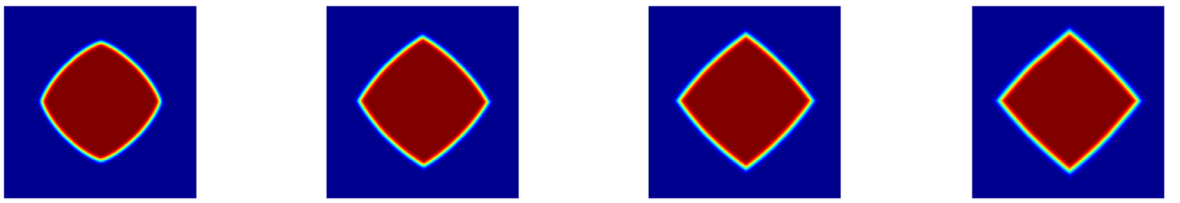

(b) 2D cross-section of $\phi(\pi,\cdot,\cdot)$ of the equilibrium solution for various α.

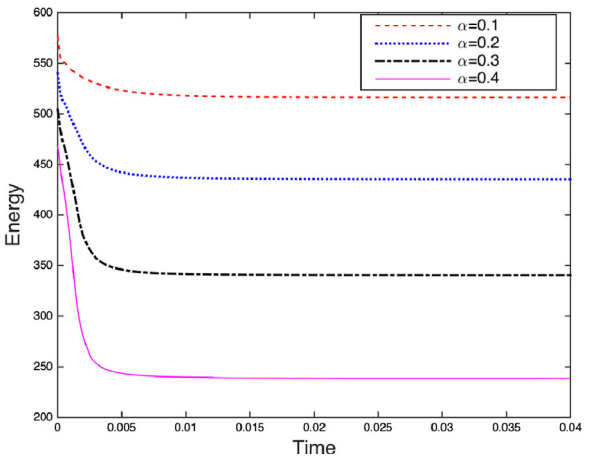

(c) Energy evolutions for various α.

Fig. 4.11. (a) Snapshots of the equilibrium solution of the anisotropic linear regularization model at $t = 0.03$ for four different anisotropic parameters α (from left to right): 0.1, 0.2, 0.3, and 0.4, respectively, by using the initial condition (4.5). (b) 2D cross-section of $\phi(\pi,\cdot,\cdot)$ of the equilibrium solution corresponding to each subfigure in (a). (c) Time evolutions of the free energy functional (2.1) for four different values of α.

Snapshots of the phase field variable ϕ are taken at t = 5e–4, 1.5e–3, 2.5e–3, and 2e–2. In Fig. 4.7(b), we show the evolution of the two free energy functionals (2.1) and (3.2) until the equilibrium. With a very slight difference, these two energy functionals decay to the equilibrium at around $t = 0.01$.

4.3.2. Anisotropic evolution of two 2D circles

In this example, we use the initial condition given in (4.2) of two circles to see how the combined effects of anisotropy and coarsening execute. We still use the defaults values of parameters from (4.1) and δt = 1e–4 for better accuracy.

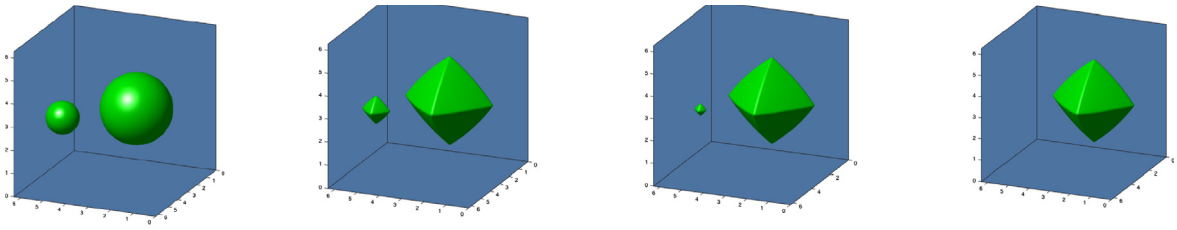

(a) Snapshots of the isosurfaces of ϕ.

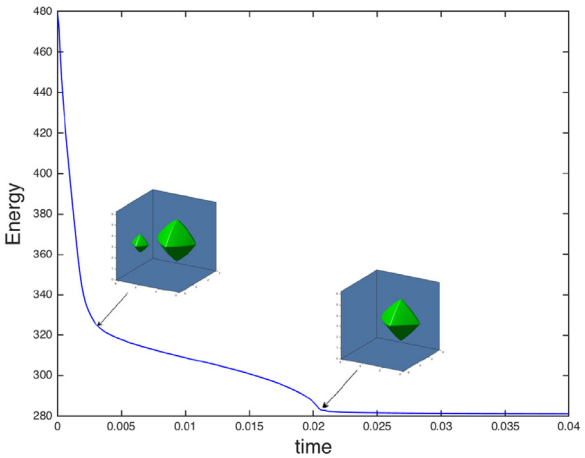

(b) Evolutions of the total free energy.

Fig. 4.12. (a) The dynamical evolution of two 3D spheres for the anisotropic model with the linear regularization, by using the initial condition (4.6) where snapshots of the isosurfaces of the phase field variable ϕ are taken at $t = 0$, 1.32e–2, 1.98e–2 and 4e–2. (b) Time evolution of the total free energy functional (2.1).

In Fig. 4.8(a), snapshots of the profiles of the phase field variable ϕ are taken at $t = 2e–3$, 9.2e–2, 1e–1, and 2e–1. We observe that the two circles first evolve to anisotropic shapes with missing orientation at the four corners, then the anisotropic system coarsens and the small shape disappears. In Fig. 4.8(b), we present the evolution of the free energy functional (2.1) until the equilibrium. The energy undergoes two rapid decreases. The first one happens at around $t = 8e–3$ when the two circles become pyramid-shape due to anisotropy. The second one happens at around $t = 9.2e–2$ when the coarsening process finishes and the small pyramid is completely absorbed by the bigger one.

4.3.3. Anisotropic spinodal decomposition in 2D

In this example, we study the spinodal decomposition for the anisotropic linear regularization model using the scheme SSAV. By considering a homogeneous binary mixture, when the spinodal decomposition takes place, the spontaneous growth of the concentration fluctuations can lead to the two-phase state. The initial condition is taken as the randomly perturbed concentration field as follows,

$$\phi(x, y, t = 0) = -0.4 + 0.001\text{rand}(x, y). \tag{4.4}$$

In Fig. 4.9(a), we perform the simulations by using the time step $\delta t = 1e–4$ and other parameters from (4.1). We observe the combined effects of anisotropy and coarsening when time evolves. The final equilibrium solution is obtained after $t = 1$, where equilibrium shape becomes a pyramid. In Fig. 4.9(b), we plot the evolution of the total free energy (2.1), which decays with the time.

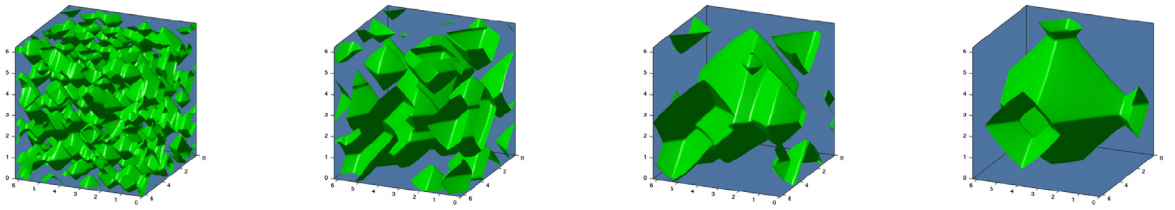

(a) Snapshots of the isosurfaces of ϕ.

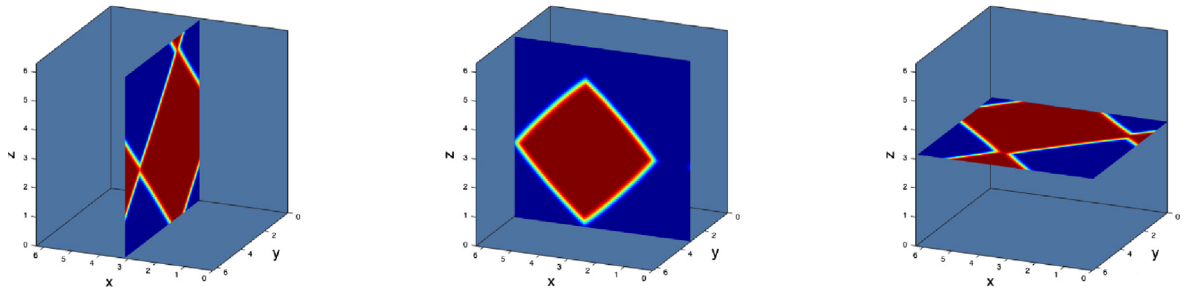

(b) From left to right, 2D cross-sections of $\phi(\pi,\cdot,\cdot)$, $\phi(\cdot,\pi,\cdot)$, and $\phi(\cdot,\cdot,\pi)$.

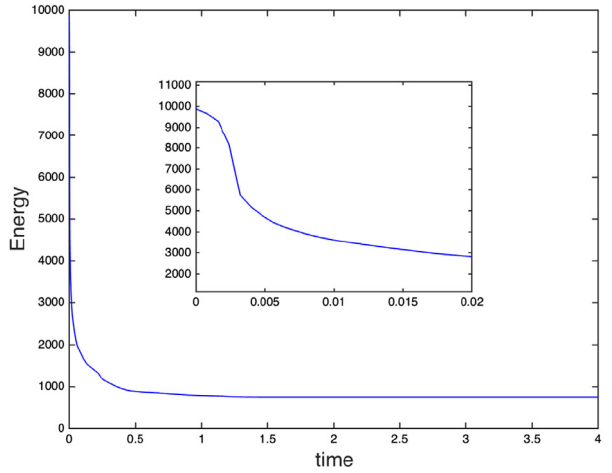

(c) Evolutions of free energies.

Fig. 4.13. (a) The dynamical evolution of the phase variable ϕ of the 3D spinodal decompositions for the anisotropic linear regularization model, by using the initial condition (4.7) where snapshots of the isosurfaces of $\{\phi = 0\}$ are taken at $t = 0.001$, 0.1, 0.3, and 4. (b) 2D cross-sections of the equilibrium solution of $t = 4$. (c) Time evolution of the free energy functional (2.1) and the small insert figure is a close-up-view where the energy decreases fast.

4.3.4. Anisotropic evolution of a 3D sphere

We next investigate the 3D simulation of a sphere by using the following initial condition

$$\phi(x, y, z, t = 0) = -\tanh\Big(\frac{\sqrt{(x-\pi)^2 + (y-\pi)^2 + (z-\pi)^2} - 1.7}{2\epsilon}\Big). \tag{4.5}$$

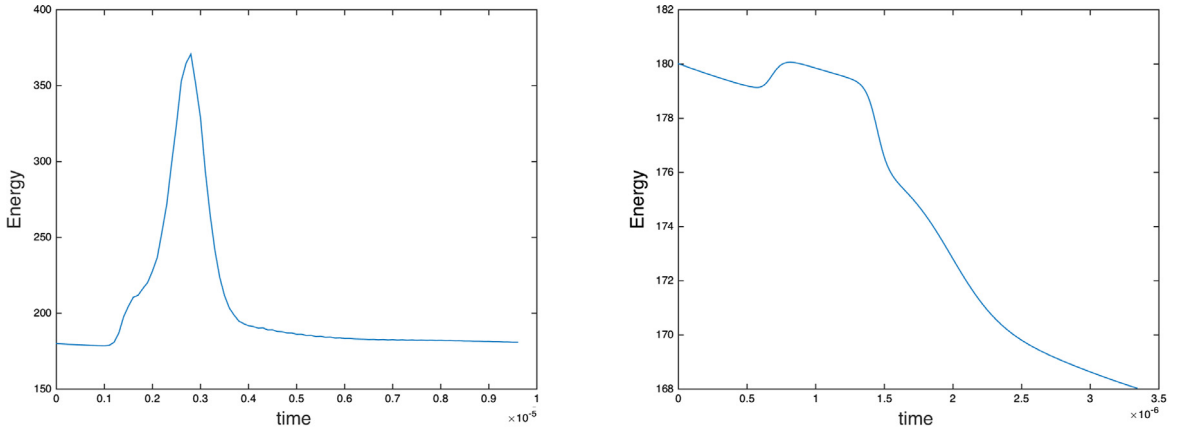

(a) Energy evolution curves computed by the non-stabilized scheme SAV-W with time step $\delta t = 1e{-}7$ (left) and $\delta t = 1e{-}8$ (right).

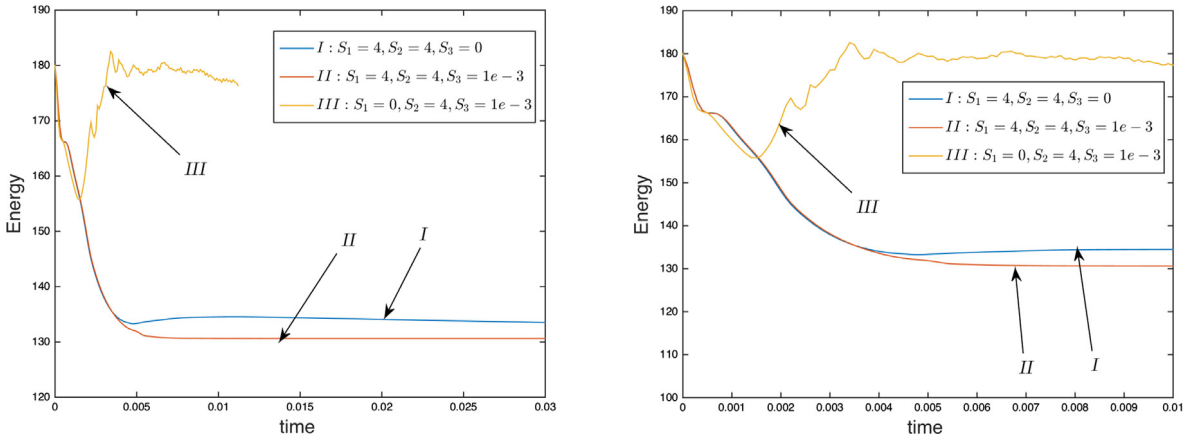

(b) Energy evolution curves computed by the stabilized scheme SSAV-W using the time step $\delta t = 1e{-}4$ and three combinations of stabilizers. The right subfigure is a close-up view.

Fig. 4.14. (a) Time evolution of the free energy functional (2.1) computed by using the non-stabilized scheme SAV-W for the anisotropic Willmore regularization model, where two tiny time steps 1e–7 and 1e–8 are used, respectively. (b) Time evolution of the free energy functional (2.1) computed by using the stabilized scheme SSAV-W and $\delta t = 1e{-}4$, where three combinations of linear stabilizers are tested. The right subfigure is a close-up view.

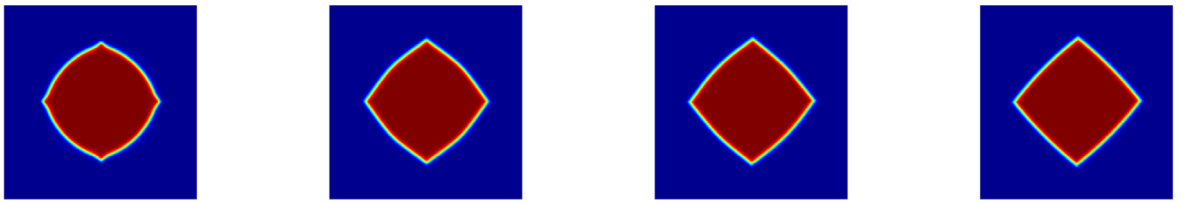

Fig. 4.15. The 2D dynamical evolutions of the phase variable ϕ for the anisotropic model with Willmore regularization, that are computed by the stabilized scheme SSAV-W with the initial condition (4.3) and $\delta t = 1e{-}4$. Snapshots are taken at $t = 2e{-}3$, $4e{-}3$, $6e{-}3$ and $3e{-}2$.

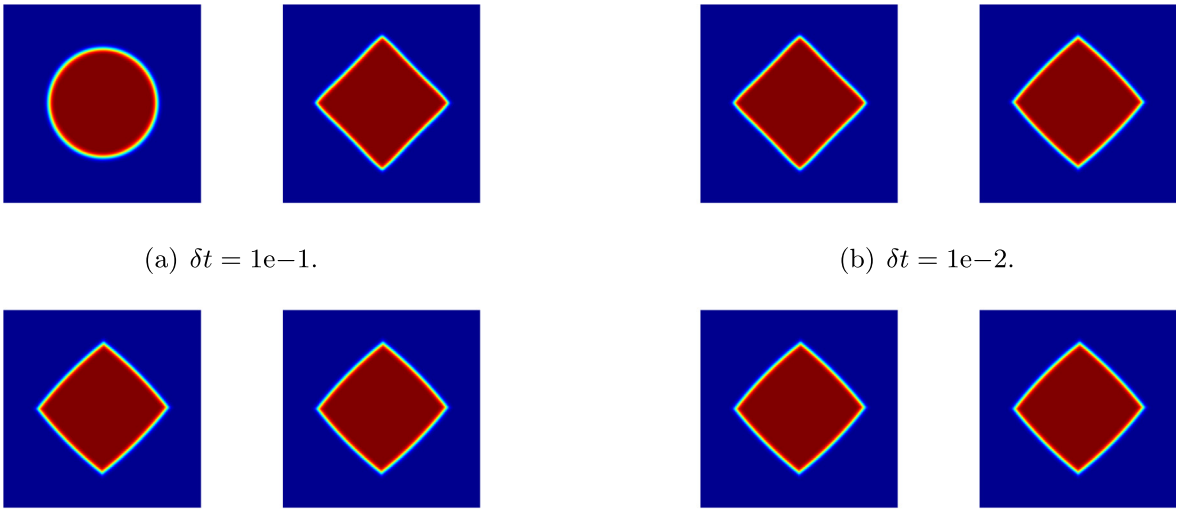

(a) $\delta t = 1\text{e}{-1}$. (b) $\delta t = 1\text{e}{-2}$.

(c) $\delta t = 1\text{e}{-3}$. (d) $\delta t = 1\text{e}{-4}$.

Fig. 4.16. Snapshots of the phase variable ϕ with four different time steps for solving the anisotropic model with the Willmore regularization with the initial condition is (4.3) computed by using the stabilized scheme SSAV-W, where (a) $\delta t = 1\text{e}{-1}$; (b) $\delta t = 1\text{e}{-2}$; (c) $\delta t = 1\text{e}{-3}$; and (d) $\delta t = 1\text{e}{-4}$. For each panel, the left subfigure is the profile of ϕ at $t = 0.2$, and the right subfigure is that of $t = 2$.

The evolution of the spherical shape towards its equilibrium is shown in Fig. 4.10(a), where we observe that the 3D sphere evolves to an anisotropic pyramid with missing orientations at six corners. Snapshots of the profiles of the isosurfaces of $\{\phi = 0\}$ are taken at $t = 1.2\text{e}{-3}$, $3\text{e}{-3}$, $6\text{e}{-3}$ and $2\text{e}{-1}$. In Fig. 4.10(b), we present the evolution of the free energy functional (2.1) until the steady state.

We further investigate the effect of the strength of the anisotropy parameter α on crystal shapes in 3D. We choose four different values of $\alpha = 0.1, 0.2, 0.3, 0.4$ and list the steady-state solutions for these four cases in Fig. 4.11(a). The corresponding 2D cross-sections along $x = \pi$ are shown in Fig. 4.11(b). When α is relatively small, e.g., $\alpha = 0.1$, missing orientations are not seen clearly. But when α increases, equilibrium shapes tend to become pyramids with sharper corners due to the strong anisotropy. In Fig. 4.11(c), we show the evolution of the free energy functional (2.1) for each α. We can observe that the energy decreases faster with larger α. The results are in very good agreement with simulations shown in [1,11].

4.3.5. Anisotropic evolution of two 3D spheres

In this example, we implement the 3D simulation of two spheres for the anisotropic linear regularization model by using the following initial condition

$$\phi(x, y, t = 0) = \sum_{i=1}^{2} -\tanh\left(\frac{\sqrt{(x - x_i)^2 + (y - y_i)^2 + (z - z_i)} - r_i}{1.2\epsilon}\right) + 1, \tag{4.6}$$

where $(x_1, y_1, z_1, r_1) = (\pi - 0.7, \pi - 0.6, \pi, 1.5)$ and $(x_2, y_2, z_2, r_2) = (\pi + 1.65, \pi + 1.6, \pi, 0.7)$.

The evolution of the two 3D spheres towards its equilibrium is shown in Fig. 4.12(a). Snapshots of the profiles of the isosurfaces of $\{\phi = 0\}$ are taken at $t = 0$, $1.32\text{e}{-2}$, $1.98\text{e}{-2}$ and $4\text{e}{-2}$. The two spheres first evolve to anisotropic pyramids with missing orientation at the six corners, then the anisotropic system coarsens and the small pyramid is completely absorbed into the larger one. The 3D dynamics are consistent with the 2D example (Fig. 4.8). In Fig. 4.12(b), we present the evolution of the free energy functional (2.1) until the steady state where two rapid decreases can be clearly observed.

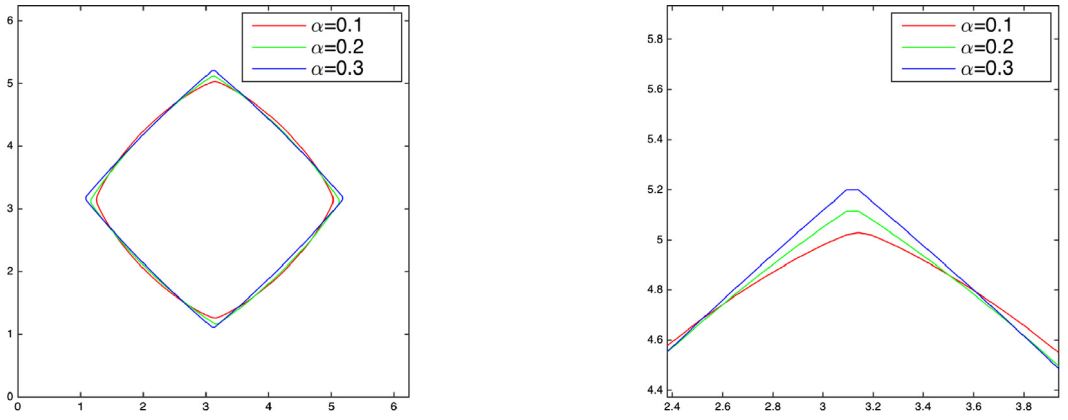

(a) The contours of $\{\phi = 0\}$ with various anisotropic strength α.

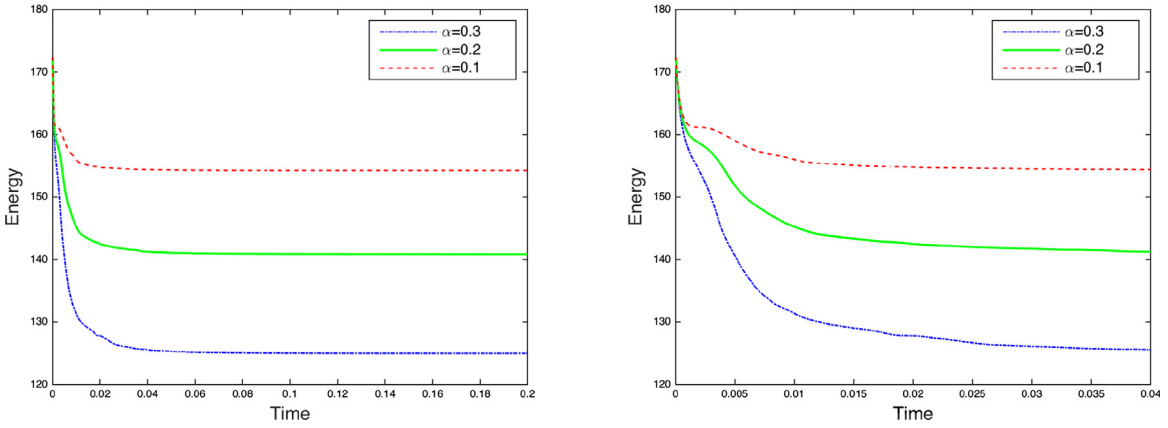

(b) Energy evolution with various anisotropic strength α.

Fig. 4.17. (a) The contours of $\{\phi = 0\}$ of the equilibrium solutions for the anisotropic Willmore regularization model by using the initial condition (4.3), $\beta =$ 6e–4 and three anisotropic strengths $\alpha = 0.1, 0.2, 0.3$. (b) Time evolution of the original free energy functional (2.1) with various α where the right subfigure is a close-up view.

4.3.6. Anisotropic spinodal decomposition in 3D

In this example, we study the 3D spinodal decomposition for the anisotropic model with linear regularization using the scheme SSAV. To be consistent with the 2D example, we use the initial condition as follows,

$$\phi(x, y, z, 0) = -0.4 + 0.001\text{rand}(x, y, z). \tag{4.7}$$

We still use $\delta t =$ 1e–4 for better accuracy and other parameters are still from (4.1). In Fig. 4.13, we present evolutions of the phase field variable ϕ by showing the snapshots of the isosurfaces of $\{\phi = 0\}$. The final equilibrium solution is obtained around $t = 1$ where it presents pyramid-like shape due to the strong anisotropy. To see the equilibrium shape more clearly, we show the 2D cross-sections of the equilibrium solution in Fig. 4.13(b). In Fig. 4.13(c), we further show the evolution of the total free energy functional (2.1).

4.4. Anisotropic model with Willmore regularizations

We consider the anisotropic system with the Willmore regularization in this subsection. To be consistent with the linear regularization model, we still use default parameters (4.1), if not explicitly specified.

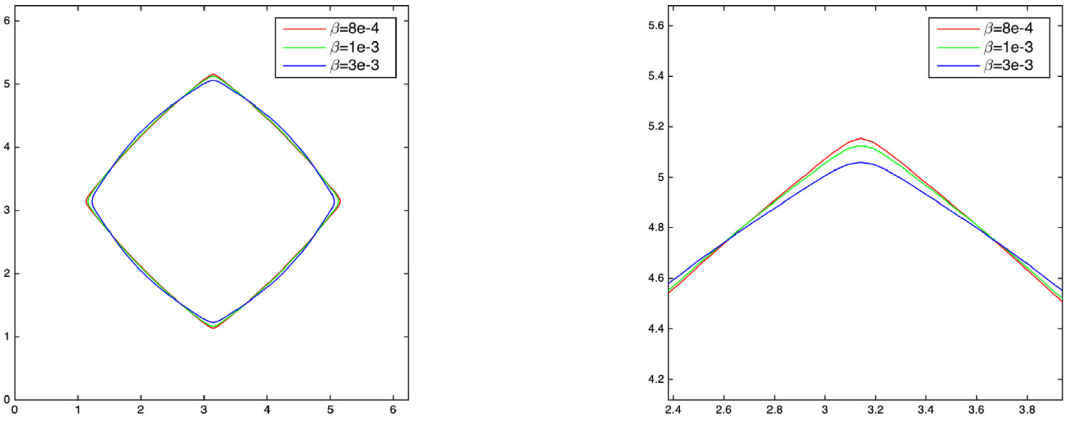

(a) The contours of $\{\phi = 0\}$ with various regularization parameter β.

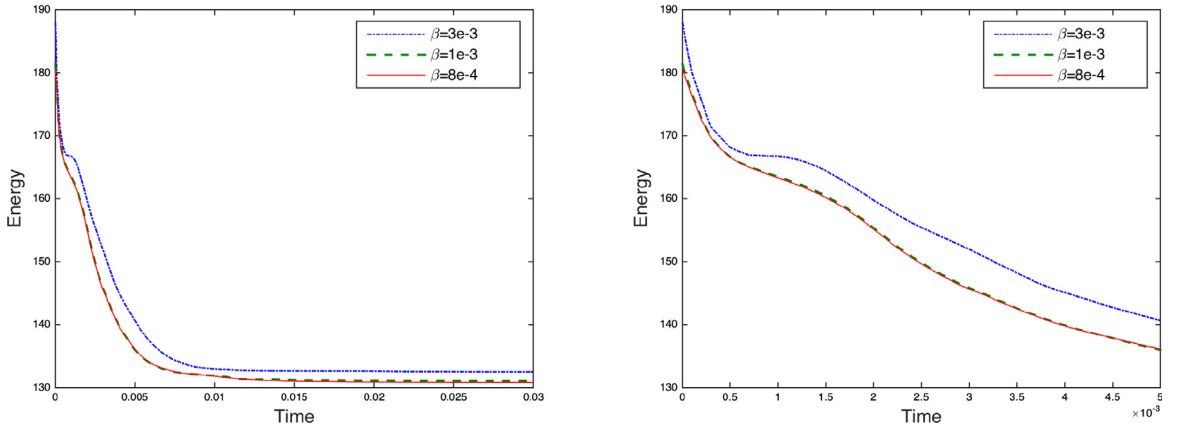

(b) Energy evolution with various regularization parameter β.

Fig. 4.18. (a) The contours of $\{\phi = 0\}$ of the equilibrium solutions for the anisotropic Willmore regularization model by using the initial condition (4.3), $\alpha = 0.3$ and three different parameters β = 8e–4, 1e–3, 3e–3. (b) Time evolution of the original free energy functional (2.1) where the right subfigure is a close-up view.

We first examine whether the non-stabilized scheme SAV-W is effective for solving the anisotropic Willmore regularization model. In Fig. 4.14, we present the time evolutions of the free energy (2.1) by using two tiny time steps, 1e–7 and 1e–8. We observe that the free energy increases even for these two tiny time steps, that implies the non-stabilized scheme SAV-W is inherently deficient for handling the anisotropic model.

In Fig. 4.14(b), with δt = 1e–4, we present the evolution of the free energy functional (2.1) for three combinations of stabilizers: (I) $S_1 = 4$, $S_2 = 4$, $S_3 = 0$, (II) $S_1 = 4$, $S_2 = 4$, S_3 = 1e–3, and (III) $S_1 = 0$, $S_2 = 4$, S_3 = 1e–3. Note there are supposed to be five more combinations of these values, however, the scheme blows up after several times of computations for them. From Fig. 4.14(b), we see that the free energies oscillate or increase with time in (I) and (III), and only the combination (II) can suppress high-frequency oscillations efficiently.

By using the scheme SSAV-W with the stabilizers in (II) and time step δt = 1e–4, we implement the simulations for the evolution of a 2D circle in Fig. 4.15. We show how the circular interface with full orientations evolves to an anisotropic one with missing orientations at four corners. Snapshots of the phase field variable ϕ are taken at t = 2e–3, 4e–3, 6e–3 and 3e–2.

We further examine if our developed scheme SSAV-W can allow large time steps. In Fig. 4.16, we show the snapshots of the phase field variable ϕ at $t = 0.2$ and 2 for four different time steps δt = 1e–1, 1e–2, 1e–3, and

1e–4. We observe that, for the two smaller time steps (e.g. 1e–3 and 1e–4), the profiles coincide very well. But for the largest time step of 1e–1 and 1e–2, the results deviate visibly away from others.

Finally, we investigate the impacts of the strength of the anisotropy strengths α and the regularization parameter β on the equilibrium of four-fold shapes. By fixing $\beta = 6e{-}4$, we choose three different values of $\alpha = 0.1, 0.2, 0.3$, and compare the equilibrium shapes in Fig. 4.17(a). We see that the increase of α leads to a pyramid with sharper corners. The evolutions of the free energy (2.1) are shown in Fig. 4.17(b), where the energy decreases faster with larger α. The effects of the Willmore regularization parameter β on the equilibrium shapes are shown in Fig. 4.18(a), in which, we choose $\beta = 8e{-}4$, 1e–3, 3e–3 and fix $\alpha = 0.3$. As β decreases, the corners become sharper in the equilibrium morphologies. The corresponding energy evolutions are plotted in Fig. 4.18(b), where one can observe that energy decreases faster with smaller β. These numerical results are in very good agreement with the results shown in [1,11,13].

5. Concluding remarks

In this paper, we have developed two fast (non-iterative), semi-discrete in time, second-order linear schemes for solving the anisotropic Cahn–Hilliard phase field model. The schemes combine the SAV approach with the stabilization technique. The novelty of the proposed stabilized SAV schemes is that all nonlinear terms are treated semi-explicitly, and one only needs to solve three linear decoupled equations with constant coefficients at each time step. More importantly, several linear stabilization terms, which are shown to be crucial to remove the oscillations caused by the anisotropy coefficients, are added to enhance the stability while keeping the required accuracy. Compared to the existing schemes for the anisotropic model, our proposed schemes that conquer the inconvenience from nonlinearities by linearizing the nonlinear terms in a new way, are provably unconditionally energy stable, and thus allow for large time steps. We further numerically verify the accuracy in time and present various 2D and 3D numerical results for numerous benchmark numerical simulations.

References

[1] S. Torabi, J. Lowengrub, A. Voigt, S. Wise, A new phase-field model for strongly anisotropic systems, Proc. R. Soc. Lond. Ser. A Math. Phys. Eng. Sci 465 (2105) (2009) 1337–1359.
[2] S. Wise, J. Kim, J. Lowengrub, Solving the regularized, strongly anisotropic Cahn Hilliard equation by an adaptive nonlinear mulltigrid method, J. Comput. Phys. 226 (1) (2007) 414–446.
[3] J.W. Cahn, J.E. Hilliard, Free energy of a nonuniform system. I. interfacial free energy., J. Chem. Phys. 28 (1958) 258–267.
[4] L.Q. Chen, Y. Wang, The continuum field approach to modeling microstructural evolution, J. Miner. 48 (1996) 13–18.
[5] J.S. Lowengrub, A. Ratz, A. Voigt, Phase field modeling of the dynamics of multicomponent vesicles spinodal decomposition coarsening budding and fission, Phys. Rev. E 79 (3) (2009).
[6] C. Miehe, M. Hofacker, F. Welschinger, A phase field model for rate-independent crack propagation: Robust algorithmic implementation based on operator splits, Comput. Methods Appl. Mech. Engrg. 199 (2010) 2765–2778.
[7] H. Gomez, T.J.R. Hughes, Provably unconditionally stable, second-order time-accurate, mixed variational methods for phase-field models, J. Comput. Phys. 230 (2011) 5310–5327.
[8] H. Gomez, der Zee Van, G. Kristoffer, Computational phase-field modeling, in: Encyclopedia of Computational Mechanics, second ed., John Wiley & Sons, Ltd, ISBN: 978-1-119-00379-3, 2017.
[9] H. Gomez, V.M. Calo, Y. Bazilevs, T. Hughes, Isogeometric analystis of the Cahn-Hilliard phase-field model, Comput. Methods Appl. Mech. Engrg. 197 (2008) 4333–4352.
[10] I. Romero, Thermodynamically consistent time stepping algorithms for nonlinear thermomechanical systems., Internat. J. Numer. Methods Engrg. 79 (2009) 706–732.
[11] F. Chen, J. Shen, Efficient energy stable schemes with spectral discretization in space for anisotropic Cahn-Hilliard systems, Commun. Comput. Phys. 05 (2013) 1189–1208.
[12] Y. Chen, J. Lowengrub, J. Shen, C. Wang, S. Wise, Efficient energy stable schemes for isotropic and strongly anisotropic Cahn-Hilliard systems with the Willmore regularization, J. Comput. Phys., https://doi.org/10.1016/j.jcp.2018.03.024.
[13] J. Shen, J. Xu, Stabilized predictor-corrector schemes for gradient flows with strong anisotropic free energy, Commun. Comput. Phys. to appear (2018).
[14] J. Shen, J. Xue, J. Yang, The scalar auxiliary variable (sav) approach for gradient flows, J. Comput. Phys. 353 (2018) 407–416.
[15] D.J. Eyre, Unconditionally gradient stable time marching the Cahn-Hilliard equation, in: Computational and Mathematical Models of Microstructural Evolution, San Francisco, CA, 1998, in: Mater. Res. Soc. Sympos. Proc., vol. 529, 1998, pp. 39–46.
[16] J. Shen, X. Yang, Numerical approximations of Allen-Cahn and Cahn-Hilliard equations, Discrete Contin. Dyn. Syst. Ser. A 28 (2010) 1669–1691.
[17] J. Shen, X. Yang, A phase-field model and its numerical approximation for two-phase incompressible flows with different densities and viscositites, SIAM J. Sci. Comput. 32 (2010) 1159–1179.

[18] Y. Gao, X. He, L. Mei, X. Yang, Decoupled, linear, and energy stable finite element method for Cahn-Hilliard-Navier-Stokes-Darcy phase field model, SIAM. J. Sci. Comput. 40 (2018) B110–B137.
[19] C. Xu, T. Tang, Stability analysis of large time-stepping methods for epitaxial growth models, SIAM. J. Num. Anal. 44 (2006) 1759–1779.
[20] Q. Huang, X. Yang, X. He, Numerical approximations for a smectic–a liquid crystal flow model: First-order, linear, decoupled and energy stable schemes, Discrete Contin. Dyn. Syst. Ser. B 23 (2018) 2177–2192.
[21] Y. He, Y. Liu, T. Tang, On large time-stepping methods for the Cahn-Hilliard equation, J. Appl. Num. Math. 57 (2007) 616–628.
[22] X. Yang, G. Zhang, X. He, Convergence analysis of an unconditionally energy stable projection scheme for magneto-hydrodynamic equations, Appl. Numer. Math. 136 (2019) 235–256.
[23] X. Yang, J. Zhao, Q. Wang, J. Shen, Numerical approximations for a three components Cahn-Hilliard phase-field model based on the invariant energy quadratization method, M3AS: Math. Models Methods in Appl. Sci. 27 (2017) 1993–2030.
[24] X. Yang, Efficient linear, stabilized, second-order time marching schemes for an anisotropic phase field dendritic crystal growth model, Comput. Meth. Appl. Mech. Engrg. 347 (2019) 316–339.
[25] J. Zhao, Q. Wang, X. Yang, Numerical approximations for a phase field dendritic crystal growth model based on the invariant energy quadratization approach,, Internat. J. Numer. Methods Engrg. 110 (2017) 279–300.
[26] D. Han, A. Brylev, X. Yang, Z. Tan, Numerical analysis of second order, fully discrete energy stable schemes for phase field models of two phase incompressible flows, J. Sci. Comput. 70 (2017) 965–989.
[27] X. Yang, L. Ju, Efficient linear schemes with unconditionally energy stability for the phase field elastic bending energy model, Comput. Methods Appl. Mech. Engrg. 315 (2017) 691–712.
[28] X. Yang, J. Zhao, X. He, Linear, second order and unconditionally energy stable schemes for the viscous Cahn-Hilliard equation with hyperbolic relaxation using the invariant energy quadratization method, J. Comput. Appl. Math. 343 (2018) 80–97.
[29] L. Chen, J. Zhao, X. Yang, Regularized linear schemes for the molecular beam epitaxy model with slope selection, Appl. Numer. Math. 128 (2018) 139–156.